SOME EFFECTS OF SECONDARY INJECTION OF GASES INTO A SUPERSONIC FLOW

Thesis by

Harvey W. Burden

Lieutenant, U. S. Navy

In Partial Fulfillment of the Requirements

For the Degree of

Aeronautical Engineer

California Institute of Technology

Pasadena, California

1964

(Submitted May 18, 1964)

ACKNOWLEDGMENTS

The author wishes to express his deepest appreciation to Dr. Edward E. Zukoski for his many valuable suggestions and his assistance in the conduct of the investigation and the preparation of the manuscript. Mr. Frank W. Spaid, who is completing his research in this same area for the degree of Doctor of Philosophy, provided many hours of fruitful discussion and helpful comments as well as providing experimental data essential to the conduct of the investigation.

In addition, a debt of gratitude is acknowledged Mrs. Robert A. Duffy for her typing of the final draft. Finally, to the author's wife, Myra, much is due for her patience, encouragement, and cheerfulness when they were sorely needed.

ABSTRACT

An experimental investigation was conducted in order to determine some of the effects of injection of a secondary stream of gas into a supersonic primary airstream. The flow fields behind an orifice producing essential two-dimensional flow and behind that producing full three-dimensional flow were studied. The resulting shock patterns, wall static pressure profiles, and flow field characteristics are described,and use is made of a theoretical injectant penetration height to non-dimensionalize the results as much as possible. It has been possible to draw some conclusions concerning the nature of the flow field and pressure field disturbances caused by secondary injection.

TABLE OF CONTENTS

LIST OF SYMBOLS

a	sonic velocity
d	injector orifice width or diameter
g	acceleration of gravity, gravitational constant
h	theoretical penetration height
$\bar{m}$	mean molecular weight
p	pressure
v	velocity
x	axial distance
y	*lateral, or cross-stream, distance*
z	vertical distance, from injector plate
C_p	specific heat at constant pressure
C_v	specific heat at constant volume
K	injectant concentration
M	Mach number
R	universal gas constant, for determination of sonic velocity
R	radial distance, for shock shapes
T	temperature
δ	boundary layer depth
γ	ratio of specific heats
θ	angular measure

Subscripts

∞	undisturbed upstream condition
0	total, or stagnation, condition
1	upstream of normal shock

2	downstream of normal shock
j	injectant jet
s	shock
A	argon
He	helium

I. INTRODUCTION

For a number of years, there has been a growing engineering interest in the effects of injecting a fluid into a supersonic stream. For many applications, the injectant fluid is also a gas which is different from the main flow. Practical applications of this procedure include thrust vector control of a rocket motor, attitude control of supersonic or hypersonic aircraft or of re-entry vehicles within the atmosphere, and fuel injection in a supersonic burner.

Numerous investigators have studied wall pressure patterns and shock profiles with a view to obtaining scaling laws for the ratio of resultant side force to primary axial thrust[1-3]. In contrast with this macroscopic approach, Zukoski and Spaid, Broadwell, and others have obtained scale parameters which enable them to reduce or non-dimensionalize wall pressure patterns which result from various combinations of free-stream Mach number, injection pressure ratio, and injectant molecular weight[4-6]. Zukoski and Spaid measured concentration profiles rather extensively and gained some insight into the mixing of the injectant with the free stream[6]. Other than these concentration measurements and some very crude total-pressure measurements by Charwat[7], no real attempt appears to have been made to study the flow field downstream of the injection port. Such an investigation could indicate quantitatively the extent and rapidity of mixing and the effects of injection upon the primary stream.

If a stream of fluid, gaseous or liquid, be injected into a

supersonic gas stream in a direction generally normal to the main flow, a shock wave system is produced. Attendant to this shock system is an interesting and useful structure of boundary-layer separation and reattachment, wall pressure patterns, velocity, total pressure, and Mach number variations, and mixing of the injectant stream with the main stream. In general, the injectant acts as a blunt body protruding into the supersonic flow; however, it has been shown[1] that injecting a fluid is more effective and feasible than using a solid object which is of the same general shape as the injectant plume's forward surface.

In this investigation, both the two-dimensional and the three-dimensional pictures are considered. The two-dimensional effects are accomplished with a slit injector across the wind-tunnel wall, while the three-dimensional effects are obtained by means of a circular orifice on the centerline of one wall. The two-dimensional system has possible application to fuel injection in a supersonic burner and attitude control devices for supersonic/hypersonic aircraft or re-entry vehicles. The three-dimensional system also has application to attitude control and, more important currently, to thrust vector control of rocket motors, either liquid or solid.

It is the purpose of the present study to provide as detailed a picture as possible of the flow field in and around the injectant plume and further downstream. In the course of this work, use was made of the concentration measurements reported by Zukoski and Spaid. Pitot total pressures were measured within the flow field and, from these, velocity and total-pressure profiles were obtained. These

then were compared with concentration profiles and other measured features of the flow.

In addition, various flow visualization techniques were used to observe the flow pattern on the wall during injection. In this way, the direction of flow and re-attachment of the separated boundary layer could be observed.

This report is divided into two main sections. The first describes the two-dimensional effects of injection and the experiment conducted to determine them. The second is composed of the same type of material pertaining to the three-dimensional effects. A summary of pertinent features is given at the end of each section, and a general flow-field description and summary is at the conclusion of the main body of text. The various sketches, photographs, and plots, and an appendix containing the general computational devices are included after the text.

II. DESCRIPTION OF EXPERIMENTAL EQUIPMENT

For this investigation, use was made of the 2" x $2\frac{1}{2}$" supersonic wind tunnel at the California Institute of Technology. Both two-dimensional and three-dimensional effects were obtained during injection of gaseous argon and helium through suitable orifices in the tunnel wall. Tunnel free-stream total pressures of one-half and one atmosphere were used at a Mach number of $2.60 \pm .02$. At one atmosphere, the Reynolds number per inch was 2.4×10^5 and the boundary layer in the test section was turbulent. At one-half atmosphere, the Reynolds number per inch was 1.2×10^5 and a laminar boundary layer was observed.

Experimental data consisted of test section conditions, Schlieren photographs, three-dimensional shock shapes during injection, secondary flow patterns in the boundary layer, wall static-pressure measurements, pitot total pressures in and near the injectant plume, and injectant total pressure.

Wall static pressures and pitot total pressures were measured with a mercury manometer bank. The injectant total pressure was measured either with a mercury manometer (low pressures) or a 1/4 percent accuracy Bourdon-Helix pressure gauge (high pressures). Secondary flow patterns in the boundary layer were obtained by spreading a mixture of instrument grease, cutting oil, and flake graphite on the tunnel wall. After a period of injection, the wall section was removed, and the flow pattern investigated.

In the three-dimensional configuration, shock shapes were

obtained from Schlieren photographs. Off-centerline shock profiles were found by positioning the total pressure probe in the shock itself. The shock position was determined by noting the dip in pitot total-pressure reading as the probe crossed the shock. The probe was then photographed and measurements taken from the pictures.

For the two-dimensional work, either gaseous argon or gaseous helium was injected through a slit orifice. This slit spanned the tunnel wall and was cut normal to the direction of flow. It was 0.006 inches wide (0.015 cm) and extended to within 1/4 inch of each wall. In Figure 1, some of the details of construction are shown. The injectant gas was fed into the plenum by two 1/4-inch tubes which, in turn, were joined by a "Y" connection to the 1/4-inch supply line. A third 1/4-inch tube was used as a pressure tap in order to record the total pressure in the plenum. A perforated baffle was added in order to disperse any directed motion of the gas as it issued from the two supply tubes, so that a uniform flow could be achieved all along the slit. A typical wall static-pressure tap is also shown; there were a number of these along the centerline of the plate. In addition, there were several taps on off-centerline planes to check the two-dimensionality of the flow. The plate proper was of brass, and the 1/4-inch tubes were constructed of copper; the static pressure taps were stainless steel tubes of 0.013-inch (0.033 cm) inside diameter.

Three-dimensional effects were obtained by injecting gaseous argon through a 0.047-inch (0.119 cm) circular hole on the centerline of one wall. As shown in Figure 2, the injection port was sup-

plied with gas directly from the 0.083-inch injector tube. This tube was of stainless steel and, in turn, was supplied from the 1/4-inch copper supply line. The plate itself again was of brass, while the pressure tap tubes were stainless steel. Several typical static pressure taps are shown. There were 65 static pressure taps arranged in various patterns on the plate in order to describe the pressure field as completely as possible.

In the two-dimensional case, wall static pressures and pitot total pressures were measured in the vertical centerline plane of the test section. Several off-centerline wall static-pressure profiles were taken by Spaid[9], and it was verified that the flow was indeed two dimensional away from the side-wall boundary layers.

For the three-dimensional jet, pressures were measured both in this centerline plane and in planes off the centerline. This was done by utilizing three-pronged rake probes with spacings of 1/8 inch and, for the shock shape determinations, 1/2 inch.

Test Section Conditions

The general characteristics and operating techniques of the GALCIT supersonic wind tunnel are described in detail by Puckett[8]. With the nozzle blocks installed for this experiment and the two injector plates used, Mach numbers of 2.58 to 2.61 were observed. The variation was due to slight differences in the plates and realignment incident to changing them. Figure 3 is a plot of normalized test-section Mach numbers for the turbulent and laminar boundary layers. It was found (Figure 4) that the boundary layer height along

the test section length was constant at about 0.5 cm for both turbulent and laminar boundary layers. Within the main flow, the maximum variation of Mach number was less than 3 per cent, and all such variations from the mean occurred quite gradually.

There were two very weak plane oblique shocks upstream of the test section caused by the joints between the nozzle blocks and the test section blocks. The variation of total head across them was about 1 - 2 per cent and, as can be seen from the angles, they are almost Mach waves. Thus, they were much weaker than the shocks caused by injection, and introduced an insignificant error. They can be seen in Figures 5, 6, and 7, and their position is also indicated on the appropriate plots of three-dimensional data. During injection, the strong bow shock almost completely overpowers this weak wave.

The parameter h, which is used throughout to non-dimensionalize distance, is a theoretical injectant penetration height. Its derivation is predicated upon the following model of the flow. The injectant is assumed to enter the flow as a sonic jet flowing normal to the main stream. This jet is allowed to expand isentropically to the main-stream static pressure within a two-dimensional or three-dimensional space, as the case may be, from which free-stream air is assumed to be excluded. In the two-dimensional case, the space is bounded upstream by a quarter of a circular cylinder, the axis of which lies along the injection slit, and downstream by a plane tangent to the cylinder directly over the slit and parallel to the tunnel wall in which the slit is located. The radius of the circular cylinder is h.

In the three-dimensional case, the space is bounded upstream by a quarter sphere whose origin is at the injection port, and downstream by a circular cylinder whose axis is along the centerline of the wall in which is situated the injection orifice and which is tangent to the quarter sphere over and cross-stream of the orifice. The radius of the sphere and cylinder is h. In each case, momentum and force balances are made in determining h. The details of derivation are given by Spaid[6, 9]. In the Schlieren pictures of the three-dimensional injection (Figures 6 and 7), the calculated penetration height of about 0.5 cm corresponds quite well with what appears to be the injectant plume's height.

In the determination of the penetration height for the three-dimensional case, a correction to the observed injectant pressure ratio was required. The pressure drop between the injectant supply line and the injection port due to fluid friction losses is the reason. In this case, it amounted to a 3 per cent reduction in injection total pressure below the supply line pressure.

order of a degree or two) that the shock is too weak to be observed readily. Whether laminar or turbulent separation occurs, the injectant protrudes into the separated boundary layer and appears as a blunt object to the main stream. Since the angle between the free stream and the forward face of the injectant surface approaches 90°, a detached normal shock is formed in front of the injectant flow. The injectant enters the flow normal to the main stream direction and immediately starts expanding in the upstream and downstream directions. It is bent downstream by the main flow and assumes the shape indicated in Figures 8 and 9.

The main flow, in going through this shock system, is deflected upward, away from the slit. Because of the rounded top surface of the injectant plume and the source itself, the area just behind the bow shock behaves approximately as a conical flow regime. The main flow which was initially bent upward and decelerated by the bow shock is gradually turned downward and accelerated somewhat. When the flow reaches the wall downstream of the slit, a second, or recompression, shock results. This is caused by the flow's having been deflected toward the wall in the conical flow area behind the bow shock. Just downstream of this second shock, the boundary layer apparently re-attaches. As would be expected, the recompression shock apparently is very diffuse in the region near the wall and does not have a well-defined point of attachment on the wall.

A slip line is present in the turbulent boundary layer case (Figure 8). This line originates at the intersection of the bow shock and the separation shock. It is caused by the difference in total head

III. TWO-DIMENSIONAL EXPERIMENTAL RESULTS

Description of Flow Field

When the injectant is introduced into the main stream through a slit in the wall which is perpendicular to the main stream, the overall effect is essentially two dimensional, since end effects are negligible. The entire flow, including the boundary layer, is required to go over the injectant surface where it issues from the slit. The protrusion of this injectant surface into the main stream establishes an adverse pressure gradient in the wall boundary layer which is felt upstream since subsonic flow exists near the wall. This causes separation of the boundary layer forward of the slit. The distance upstream and the nature of the separated profile depend upon whether the boundary layer is laminar or turbulent prior to separation. The dependence of the flow field geometry on the state of the boundary layer is illustrated in Figures 5, 8, and 9. Figure 5 is a Schlieren photograph taken when the free-stream total pressure was one atmosphere and the boundary layer was turbulent; Figure 8 is a sketch of the flow field. The laminar boundary layer separation, at one-half atmosphere, was not readily observable on the Schlieren photographs; Figure 9 is a sketch of the flow field.

The abrupt increase in boundary layer thickness at separation looks like a ramp to the remainder of the flow, and an oblique shock results. This, as mentioned above, is observed for the separation of the turbulent boundary layer, but not for the laminar; the angle formed at laminar boundary-layer separation is so small (of the

between the two flow areas which proceed through the bow shock; the flow above the intersection has full free-stream total head, whereas the flow below the intersection has had its total head diminished in passing through the separation shock. The slip line results where the two flows of different velocity must meet.

Discussion of Results

During injection of gaseous argon (and, in one case, gaseous helium) through the two-dimensional orifice, wall static pressures and pitot total pressures at various axial and vertical (total pressure) stations were recorded. Spaid[9] has made pressure measurements on off-centerline planes and found that the pressure pattern is indeed two-dimensional in nature.

A series of wall static pressures were obtained at each injection condition studied. All of the profiles were quite similar to that shown in Figure 10, with the exception of the upstream portion of the laminar boundary layer case. In the turbulent case illustrated, the the rise in static pressure at $x/h = -10$ is due to the separation of the boundary layer and the resulting separation shock. The continued increase in pressure is due to the interaction of the bow shock and the boundary layer. The bottom of the bow shock intersects the boundary layer at about $x/h = -3$. In the laminar case, the initial increase in pressure occurs much farther upstream, about $x/h = -30$, and is considerably smaller in magnitude. There is a gentle rise until the bow shock - boundary layer intersection is reached, and then the characteristic large rise in pressure is seen. The

downstream profiles with a turbulent or a laminar boundary layer are almost identical.

The pressure behind the injector has a minimum value of about 0.3 p_∞, and at x/h of about 3 starts to rise to the mainstream value, p_∞. The recompression zone covers the region $3 \leq x/h \leq 7$. This downstream region described here is quite similar to that found downstream of a rearward facing step at Mach number 2.6. That is, the pressure minimum is between 1/4 and 1/3 of p_∞ and the recompression zone geometry is similar.

The total pressure data were obtained throughout the flow field downstream of the recompression zone. Since the flow is supersonic, the pitot total pressures must be corrected to take into account losses which occur at the bow shock which exists in front of the probe inlet. The Rayleigh formula (equation 6-3 of reference 10) was employed. Because concentration data had been obtained by Spaid[9], account could be taken of the change in ratio of specific heats due to varying concentrations of injectant. It was assumed that the static pressure was constant vertically up to the recompression shock (Figures 5, 8, and 9), and equal to that measured along the wall (Figure 10) at the appropriate position. As can be seen from Figure 10, the most forward station at which this assumption could be made is about x/h = 6.

The stations investigated here correspond to those for which concentration profiles were available from Spaid[9]. For some of the data (Figure 11), account was taken of the change of static pressure across the recompression shock and, since conical flow seems to exist between the shocks, a linear variation of static pressure be-

tween them was assumed. The static pressure behind the bow shock was found from known free-stream conditions and the measured shock angle. The Mach number and flow direction were not known in front of the recompression shock, but they were known behind it from the Rayleigh supersonic pitot formula solution and the wall boundary condition. By an iterative process involving matching the recompression shock angle from the wall and Mach number just downstream of the shock with possible Mach number and flow direction combinations just upstream of the shock (figures 2-1 and 2-7 of reference 11), the upstream Mach number was found. Thus, the static pressure jump across the shock could be calculated giving the static pressure at the bottom of the conical flow regime. The flow direction just before the recompression shock was found to be $32 \pm \frac{1}{2}^{o}$ into the wall. This correction was not made in most of the data (Figures 12, 13, 14, and 15), so the computed results above the indicated position of the recompression shock could be in error by as much as 10 per cent. The injectant concentration, however, is usually close to zero in this area, so the error does not materially affect the results of this investigation.

With the static pressure thus determined in the area of interest, the Rayleigh supersonic pitot formula was applied graphically, taking into account the injectant concentration. From the Mach number and the ratio of specific heats, the ratio of total to static temperature was calculated. The total temperature was assumed to be constant at room temperature, 530^{o}R. The local speed of sound for the appropriate injectant concentration was calculated and then the

local velocity found. In addition, the ratio of total pressure to free-stream total pressure was calculated. The specific formulae, tables, and curves used are shown in Appendix A.

The data treated in this manner are presented in Figures 11 to 15 for a range of test conditions. Plots of total pressure, concentration, and velocity are presented as a function of distance from the wall for stations 6.67, 14.7, and 30.8 h downstream of the injector.

For Figure 11, the flow field was measured in considerable detail. This then gives a good basis from which to study the effects of varying injection pressure ratio (Figures 12 and 13), boundary layer condition (Figure 14), and injectant molecular weight (Figure 15) as well as the characteristics of the flow itself. From the data related to Figure 11, a mass continuity check on the argon at the three stations was performed. The foremost and aftmost were within 1.2 per cent, while the center station was 15.1 per cent higher than their mean. This is considered to be a good check of the calculations in spite of the difference at the center station.

Mixing of the argon with the air is seen to occur smoothly and fairly quickly. The velocity increases rapidly to mean free-stream magnitude, and by the aftmost station the well-established boundary layer profile is present. The boundary layer thickness here is the same as the free stream value, about 0.6 cm. The total pressure suffers somewhat in passing through the bow shock and even more through the recompression shock. It recovers to almost free stream value at $x/h = 30.8$; the deficit is that experienced in going through both shocks in this case. The very low total pressure near the wall

is due to a combination of being in the boundary layer and the larger amounts of injectant present. Since the argon initially entered the tunnel normal to the stream, it had no momentum axially, and any it gained was due mainly to mixing with the free stream. The overshoot of total pressure ratio at $x/h = 6.67$ at the higher values of z/h indicates that the assumption of conical flow between the bow and recompression shocks was not completely justified that close to the slit. Further aft it appears satisfactory.

By comparing Figures 12 and 13 with Figure 11, the effects of varying injection pressure ratio, and thus the penetration height, can be deduced. As was noted by Spaid[9], the relative effectiveness of injection appears to decrease as the injectant penetration height approaches the boundary layer depth. That is, as h/δ increases (δ, the boundary layer depth, being constant), the injectant concentration penetrates to a decreasing z/h height. This can be seen by comparing Figure 11 with Figure 12, where the penetration height, h, is decreased, and with Figure 13, where it is increased. The z/h height of, say, the 30 per cent concentration point steadily decreases as h increases. It is to be noted, however, that the concentration at the wall remains constant. This clearly indicates that h is not the perfect scaling parameter for these purposes; rather, it should increase a little less rapidly with injection pressure ratio. Velocities and total pressures follow the same general pattern as the concentration profiles with the exception that their values above the indicated position of the recompression shock are not accurate. This is so, since the jump in static pressure across the shock was not ac-

counted for in computing the velocities and pressures in Figures 12, 13, 14, and 15.

The dependence of injection pattern on the ratio h/δ is reasonable. For $h \ll \delta$, the forces acting to turn the injectant flow are generated by the impact of relatively low energy flow of boundary layer gases. However, as h approaches δ, the energy of the primary stream material turning the injectant increases rapidly, and it is to be expected that h will then increase more slowly.

The effect of having a laminar boundary layer instead of a turbulent one can be seen by a comparison of Figures 11 and 14. There is very little difference between the respective profiles. The velocities are almost exactly alike. The mixing, indicated by concentration and total pressure, appear to proceed more at higher levels into the flow, but the differences are not large. The increase in penetration of argon into the main stream is probably due to the weakness of the shock off the boundary layer separation streamline. This means that all the flow entering the bow shock is essentially at free-stream total pressure, so that there is a uniform drop with no slip line. The less energetic air, relative to that existing in the turbulent case, close to the wall alows the injectant to penetrate further into the stream. In addition, the thickness of the separated laminar boundary layer at the injection point is greater than that of the corresponding turbulent layer. This effect should also produce an increase in the penetration height.

Comparison of Figures 12 and 15 illustrates the effect of different injectant molecular weights. Here, there is little or no effect

upon the velocities or total pressures, but the concentration profiles are markedly different. This is explained by noting that a considerably lower mass flow of helium than argon was required to produce similar physical effects at the same h . Note that the physical flow, velocity, and total pressure, are nearly identical, as are the penetration heights, h . The calculation of h involves the reciprocal of molecular weight, and this verifies the derivation in this respect.

Summary

The salient features of the effects of this two-dimensional case can be summarized briefly as follows:

1. The entire flow upstream of the injector is required to go over the injectant plume much as it would over a solid, thin, rectangular plate standing normal to the wall.

2. The wall static pressures produced are quite similar to those produced by such an obstruction, especially downstream.

3. Mixing and diffusion of the injectant with the main stream air proceed smoothly and fairly rapidly.

4. As the ratio of penetration height to boundary layer thickness (h/δ) increases, the relative effectiveness of injection in producing useful pressure forces is reduced.

5. The bow shock shape is rather insensitive to the state of the boundary layer upstream of the injection slit. The pressure patterns downstream and the recompression shock are almost entirely independent of it.

IV. THREE-DIMENSIONAL INJECTION EXPERIMENTAL RESULTS

Description of Flow Field

The three-dimensional injection effects were investigated essentially for one injection ratio and one Mach number. Zukoski and Spaid[6] developed the scale parameter, or calculated penetration height, h , which was described previously. They found that h is a very good scaling parameter. For this reason, a complete definition of the flow field in terms of normalized quantities and distances made non-dimensional by h for a few test conditions should give a good description of all similar flow fields. The conditions chosen for intensive study here are $M = 2.61$ and $p_{o_j}/p_{o_\infty} = 7.77$.

To obtain the three-dimensional effects of injection, a point-like source, in the form of a circular orifice, is used. Since there is only a partial blockage of the main stream flow and boundary layer here, the resulting flow field is able to develop in all directions above the wall. The injectant, instead of blocking the boundary layer entirely, passes through it and expands in a plume which remains primarily off the wall and may be above the boundary layer. The surface which it forms in passing through the boundary layer is essentially an inverted frustrum of a cone, the small end resting on and coinciding with the injection port.

The resulting plume is then bent back to a flow direction parallel to the plate by the interaction with the main flow. General pictures or sketches of the flow are shown in Figures 6, 7, 16, and 17.

The most prominent features of the flow shown here are the bow shock waves. Near the intersection of this shock and the wall is the complex separation region.

Boundary Layer Separation

Since the injectant passes through, rather than blocks, the boundary layer, the resulting adverse pressure gradient in the boundary layer is a local phenomenon restricted to a region just upstream of the injection port. Both turbulent and laminar boundary layer separation are observed. The separated regions can be seen quite easily in Figures 6, 7, 16, and 17, where the difference between separation of the turbulent and laminar boundary layers is also evident. The greater upstream separation distance in the laminar case is the result of the laminar boundary layer's lower resistance to separation when under the influence of an adverse pressure gradient. The great difference in separation angles is also shown here; the laminar angle is always less than 5°, whereas, in the turbulent case, the angle is as large as 30°. In the turbulent boundary layer case, an oblique shock is set up by the separation of the boundary layer; in the laminar case, this oblique shock is present, but is too weak to be observed.

When the injectant plume reaches the main stream and expands, the detached bow shock is formed which becomes weaker as the distance from the injection port is increased.

Note again that the first two oblique shocks which look like separation shocks are caused by slight imperfections in the wall. See page 7.

Shock Shape

A three-dimensional picture of the shock shape was obtained in the following manner. At three different injection pressure ratios, and thus at three different values of h , the vertical and horizontal positions of the shock were measured. This was done by noting the dip in pitot total pressure as a pitot probe passed the shock and then measuring the probe position from a photograph. These measurements were compared with the shock shape determined from a Schlieren photograph of the shock at the same axial (x) station and on the same photograph. Comparison of these measurements indicated that the shock surface is axisymmetric about a centerline which is one h from the wall. Figures 18a and 18b illustrate this. In these figures, $(z_s - h)$ is the height of the shock, measured from the axis line which is one h off the wall, as measured from the Schlieren of the shock shape. R is the computed radial distance to the point at which the pitot probes met the shock measured from the same axial line one h off the wall. Both distances are normalized by h in these figures. The correspondence is within $\pm$ 4 per cent except for two points, which are apparently due to auxiliary cross-flows at that tunnel condition (laminar boundary layer) caused by boundary layer separation on the tunnel side wall.

Shock shapes as measured above are also compared with those measured from the Schlieren photographs (indicated as reference) in Figure 19. The coordinate x' is the axial distance from the front of the bow shock instead of the distance from the injection orifice used elsewhere in this report. The correspondence is seen to be excel-

lent. The maximum deviations are due to the above mentioned flow anomalies.

In these tests, the boundary layer is about 0.5 cm thick. It is felt that the correlation of the data shown in Figures 18 and 19, with the axis of symmetry located at h off the wall, indicates that h and not the boundary layer thickness is the proper distance for the location of the axis of symmetry. Use of $\delta = 0.5$ cm instead of h as the offset distance for the axis leads to systematic errors in the correlation of shock coordinates for the two higher values of h .

Flow Patterns in Boundary Layer

Further indication of the flow pattern was obtained by examination of the secondary flow pattern in the boundary layer on the wall. A mixture of instrument grease, cutting oil, and flake graphite was spread on the injector plate, and injection pressure ratios of 7.77 and and 30.2 were used to gain a physical picture of the flow patterns on the plate. Figure 20 is a sketch of the flow pattern at $p_{0_j}/p_{0_\infty} = 7.77$, and Figure 21 is a photograph of the plate itself after the run was made. In the sketch, Figure 20, typical streamlines are shown. The first heavy line is the locus of points at which non-axial flow first occurred; it is thought that this boundary represents the line along which boundary layer separation starts. The second heavy line is the locus of points along which a second abrupt change in flow direction occurs. It is judged to be the line at which the wall static pressure is a maximum and hence is the intersection of the bow shock with the separated boundary layer. If the axisymmetric shock shape were drawn on this sketch, it would fall about one boundary-layer depth outside this

shock - boundary layer intersection curve. Thus, it falls in region 1. It is felt that when the bow shock hits the top of the boundary layer, it creates a lambda structure, as seen from the side, with one leg bending toward the orifice and the other away.

After the secondary flow passes through the bow shock and is turned, it exhibits a definite and strong flow toward the axis. Near the orifice and behind it, there is a back flow which was visible during the run by its effect upon the grease mixture. The grease could be seen being swept forward and piled up in a small mound directly behind the orifice at the vertex of the V-shaped region, region 3. This mound of grease was blown downstream by the collapsing flow when the tunnel was stopped, and hence does not appear in Figure 21. After crossing the V-shaped curve, bounding region 3, the flow proceeds essentially axially. The angle formed at the vertex is about 15°. At the far aft end of the plate, the flow appears to be turned into the centerline by about 7°. The most obvious interpretation of the V-shaped boundary is that it is a wake shock caused by the impingement of the two flows which have gone around the sides of the plume. However, near the body, or around $x/h = 2$, the flow picture is confused and the boundary may only be an indication of the recirculation pattern.

This same technique was used at a pressure ratio of 30.2 and a laminar boundary layer. The same general pattern was seen except that boundary layer separation took place at or upstream of the front edge of the plate. Consequently, only one curve, the bow shock - boundary layer interaction, was seen around the orifice. The same

V-shaped region was present downstream, and the flow pattern, from the lines in the grease, was qualitatively similar.

The flow pattern in region 2 suggests that two vortices are shed from the obstacle formed by the injection process. Their presence is indicated here by the strong inflow suggested by the streamlines of secondary flow in this region. In addition to this data, examination of concentration data obtained by Zukoski and Spaid[6, 9] also indicate that vortices are attached to either side of the injectant plume. They are apparently arranged in such a manner that air from the free stream is swept from outside the plume into and under it. These induced flows meet on the centerline and produce an upward motion there. As observed from upstream, the right vortex rotates clockwise, and the left vortex counterclockwise. The effects of this can be seen quite clearly in the concentration and total pressure profiles to be discussed later.

Static Pressures

Typical variation of static pressure with distance from the injector is shown in Figure 22. Upstream of the injector, the wall pressure rises rapidly due to separation and the bow shock; downstream, the pressure is very low and gradually rises to the free stream value at about 4h . These data are for the centerline of the flow; off the centerline, static pressures rise more slowly and do not reach the free-stream value until about 8h .

The low-pressure region downstream of the injector is apparently a region of flow separation, and the gradual rise in pressure suggests that the flow becomes reattached to the wall in this region,

that is, $2 \leq x/h \leq 4$.

An attempt was made to find the re-attachment point of the flow by a direct method. A pitot probe was advanced along the wall while the measured pitot total pressure was compared with corresponding wall static pressure from the static-pressure taps. When the two were just equal, re-attachment would be indicated. This was attempted at injection pressure ratios of 7.77, about 10, and about 15. The results were not very precise, but it appeared that re-attachment starts at about $x/h = 2$. This corresponds fairly well with conclusions drawn from wall static pressure plots[6, 9]. The off-axis pressure data also suggest that the re-attachment region is connected with the weak shock bounding region 3.

Comparison of the secondary flow patterns, Figure 20, and static pressure measurements such as those shown in Figure 22 confirm the general features of the flow discussed in connection with Figure 20. This agreement is shown in more detail by the pressure contour map of Figure 23. Here, the contours have been drawn through all the static pressure data which were available along cuts at $y/h = 0$, 1.2, 2.2, and at $x/h = 1.2$ and 2.3. Although considerable imagination was used in certain areas, the map is in good qualitative agreement with the observations. The map shows the pressure rise along the boundary of region 3 and suggests again that downstream of $x/h = 2$ this boundary is a shock wave which straightens out the vortex-like flow which is converging on the centerline from either side of the injector. In addition, the adverse pressure gradient in the separated region, region 1, and the pressure peak along the boundary

between regions 1 and 2 are clearly shown. The pressure peak at $3 \leq x/h \leq 4$ is apparently due to the interaction of the weak recompression shock, which bounds region 3, and the flow in the wake. Thus, this region is similar to the neck and wake shock found in supersonic flow behind two-dimensional blunt bodies held normal to the flow.

Total Pressure and Velocity Profiles

In general, the same technique was used to obtain the total pressure and velocity profiles as was used in the two-dimensional case. Again, the wall static-pressure data were used to determine the velocity.

It was found (Figure 23) that the static wall pressure approached the undisturbed flow value by $x/h = 4$ along the centerline but not until $x/h = 8$ at off-axis stations since the outboard probe was at $y/h = 1.22$.

Thus, the station $x/h = 8$ was the most forward one at which the static pressure could be assumed constant vertically into the flow at all positions off axis. This pressure was required in order to apply the Rayleigh supersonic pitot formula. Pitot static pressures were measured at various axial stations downstream of $x/h = 8$ and vertically into the flow. A three-pronged rake probe was used so that centerline and two off-axis pressure readings were taken at each probe position. These pitot total pressures, the respective static pressures, and concentration profiles taken by Spaid[9] were applied to a graphical solution of the Rayleigh supersonic pitot formula. The

same technique was used here as was used in the two-dimensional calculations discussed earlier. Since concentration data were available at slightly different axial positions from those used here (5.77 and 11.81), interpolated profiles were used. The results of these calculations are plotted in Figures 24, 25, 26, and 27, where the interpolated concentration profiles are also shown. The Mach numbers are shown only in Figure 24, since they have the same relationship to V/V_∞ in all cases. The undisturbed boundary-layer profile is plotted in Figure 26 to illustrate the effects of injection. The indicated shock positions are those of the shock from the crack between the nozzle block and the injector block. They are not the bow shock; in no case was it reached by the probe.

The concentration profiles (Figures 24, 25, 26, and 27), when compared at centerline and off-centerline stations, illustrate the effect of the two vortices in lifting the plume in the center. This is illustrated even more clearly in Figure 28, discussed below. It is seen that as the plume proceeds downstream it remains within about the same vertical boundary, diffusing upward only slightly. Its cross-stream extent remains fairly constant. Near the centerline, the vertical position of maximum concentration also increases somewhat, while cross-stream, it decreases. This again indicates the vortex motion. Consider Figure 24. At the centerline station, $y/h = 0$, the total pressure, velocity, and Mach number near the wall have been reduced considerably below free-stream conditions because of the shock system and the obstruction of the injectant plume itself. The peaks near the wall and at the outer edge of the boundary layer are

due to the fresh, energetic air swept in by the vortex motion. Note that the boundary layer height here is only about one-half of the undisturbed value.

Above the boundary layer, the total head decreases to a minimum and then starts increasing toward near free-stream values. The decrease and very low value of total head at the minimum are due to several factors. First, if the free stream had suffered a simple normal or near-normal shock, the total pressure would only have been decreased to about one-half of its former value. With the injectant entering at a total head ratio of about 8 , it would be expected that, if anything, it would produce a slight increase upon the reduced (to about one-half) total pressure profile, even with the right-angle turn the injectant makes. Since the ratio of injectant mass flow to main stream mass flow is of the order of several per cent, this increase, albeit a localized effect, would not be extremely great, but it would at least be an increase. However, the measurements show a decrease in this same area. The other factor which must be considered here, and which explains the drop in total head, is the aspiration effect of the injectant jet upon the boundary layer. Just as an eductor, the jet carries the adjacent boundary-layer air up with it. Since the boundary layer is separated downstream, a considerable backflow up to and up with the jet results. This flow was observed in the grease experiment. This very low energy boundary-layer air mixes with and degrades the energy of the injectant. Instead of the simple, normal shock system upstream, there is a rather complex shock structure which tends to decrease the total head even more. The sum effect is

the dip in total pressure which is observed. In addition, the back flow due to the aspiration effect tends to feed and maintain the vortices.

Note that the minimum points of total pressure, velocity, and Mach number approximately coincide with the peak of the concentration profile. This correspondence is a result of the above described mixing of the injectant jet and the separated boundary layer.

Beyond the area of maximum injectant concentration, the total head steadily increases toward the free-stream values. Above the plume, the flow has passed through the upper part of the bow shock. This upper part is seen to have a more acute angle than the lower portion and is not so strong; hence, the total pressure approaches more closely the upstream value.

In the cross-stream direction, the effect of boundary layer entrainment is seen to persist practically undiminished out to $y/h = 0.6$, but the boundary layer itself has not been affected nearly so strongly by the jet. At $y/h = 1.2$, the flow has not been seriously affected by injection, and the extreme limit is probably about $y/h = 1.5$. The boundary layer at $y/h = 1.2$ is close to the undisturbed profile (Figure 26 emphasizes this); thus, it can be seen that the plume itself possesses somewhat of the axisymmetric shape, one h off the wall, which the bow shock was shown to have, with the exception of the dip to the plate near the centerline plane (much as a stand or support).

As the flow proceeds downstream (Figures 25, 26, and 27), the boundary layer is seen to redevelop until it reaches its former

level of about 0.5 cm near the $x/h = 12$ station. The effects of the jet's mixing are seen to diminish as the flow progresses; however, the containment of the injectant by the vortices along the centerline plane appears to persist rather strongly. At best, it can be said that there is a very complex flow field within and around the injectant plume. The complex nature of the flow field apparently does not simplify itself very rapidly; even at $x/h = 12$ or 15, it is far from uniform except above the plume.

Figure 28 is a comparison plot of argon concentration profiles and total pressure-ratio profiles at $x/h \approx 12$. The concentration profiles are from reference 9. In this plot, the very direct relationship between injectant concentration and total pressure within the plume is seen. Note that the area of minimum total head corresponds almost exactly with that of maximum argon concentration. Conversely, the total head increases toward free-stream values outside the plume when concentrations approach zero. The effect of the two vortices in sweeping fresh, high total head air under and into the plume can be observed above the boundary layer.

The boundary layer is seen to have recovered its former, undisturbed height of about one h ; at the upstream stations it was as low as one-half h . The contour of total head in the boundary layer is the normal one expected except on the centerline plane where the lifting effects of the two impinging vortex flows is evident. The low total head near $z/h = 2$ is a combination of the low-energy boundary-layer air which is swept up and contained by the vortices and the injectant itself, which lost a considerable amount of its energy in being turned

so abruptly through a right angle. Note that the disturbed region is roughly circular in cross section, with a center at about 1.7 h and a diameter of about 2.6 h. At x/h of about 1.6, concentration data (Spaid[6]) show that the diameter is about 2h and the center is about h above the wall. Hence, it is evident that the spreading rate of the disturbed region is very slow.

At this axial station ($x/h \approx 12$), the axisymmetric shock has a radius of 7.94 h with the origin at $z/h = 1$ from the wall. The areas of significant injectant concentration and reduction of total pressure are well within the shock envelope.

In addition to the measurements described above, pitot total pressures were measured at three axial positions between the orifice and the $x/h = 8$ station. Since, in this area, there are quite large static-pressure gradients both in the axial and the cross-stream directions, the assumption of constant static pressure vertically could not be made. Nevertheless, these pitot total pressures follow the same general pattern as those which were reduced. This can be seen in Figure 29, where they are plotted along with the corresponding pitot total pressures from station $x/h = 8$, which is the most forward station for which computations were made. Particularly at $x/h = 2$, there is some doubt that the complete pitot total pressure was indicated, since it is known that the injectant issuing from the orifice causes widely varying flow directions within the plume near its origin.

The fact that the pitot total pressures very close behind the injection orifice (0.9 cm) were of the same pattern as those discussed above is interesting. It indicates that the general pattern of the flow

field is established very quickly after the injectant enters the stream. As pointed out previously, this pattern persists beyond the limits of measurement in these experiments, or $x/h = 15$. The very low values of pitot total pressures near the wall close to the orifice indicate the separated and reverse flow which was actually observed in the grease film experiment described earlier.

The increase of pressure through the boundary layer and then the dip close to the vortices is of the same pattern as further downstream. Particularly at $x/h = 1.75$, the rapid rise in total pressure as the probe moved through the injectant jet (which at this point is still quite energetic) is apparent.

Summary

The most important effects of three-dimensional injection as investigated herein can be summarized as follows.

1. The injectant plume penetrates through the boundary layer and into the main stream, essentially allowing the boundary layer to flow under and around it.

2. The bow shock standing upstream of and above the plume is axisymmetric in shape. Its axis is a straight line lying in the centerline plane and parallel to the tunnel wall at a height of one h.

3. Two vortices are shed from the top front area of the plume. These vortices are associated with considerable back flow along the wall behind the injection port.

4. The above-mentioned vortices and back flow aid in mixing of the injectant at the boundaries of the plume, but somewhat contain

it also. Mixing progresses less rapidly than in the two-dimensional case.

5. The parameter h appears to be a good scaling parameter for shock shapes as well as for wall pressure profiles. This is in spite of the complex nature of the shock systems and flow field.

6. The shock shapes and downstream pressure patterns, indeed the total pressure patterns, are quite insensitive to the state of the boundary layer upstream of the injection port.

V. CONCLUDING REMARKS

The flow field which is produced by secondary injection has the following general features. When the secondary flow is introduced, it appears to the main stream of gas as a blunt object. A shock wave is produced with the forward portion being a normal or near-normal detached shock and the upper portion an oblique shock of gradually decreasing strength. The main flow which passes through the upper part of the oblique shock is little affected by it; however, that part traversing the lower part is greatly decelerated and deflected. This decelerated flow is then required to make its way through and around the injectant plume; this results in rather rapid mixing and diffusion of the injectant gas into the main gas flow.

The presence of the injectant jet and the interaction of the bow shock with the boundary layer cause an adverse pressure gradient in the boundary layer, which, in turn, cause separation. In both types of boundary layers (turbulent or laminar), the separation forms an effective ramp, and a shock results forward of the bow shock at the point of separation. Since the turbulent separation occurs later and forms a larger effective ramp angle, the separation shock in this case is considerably stronger and more readily observable than in the laminar case. The separated boundary layer re-attaches within a moderate distance downstream of the injection orifice, and it quickly re-establishes its former depth and profile. The state of the boundary layer upstream of injection has little effect upon the flow field downstream except in the severity of oblique separation shock which the main flow traverses prior to meeting the bow shock.

In the case of an injectant line source across the direction of main flow, the flow field is essentially two-dimensional in nature. The entire flow, after passing through the bow shock, is required to go over the injectant plume in one direction (the vertical) as well as partially through it. This ensures rather rapid mixing of the two streams, especially at the top of the plume. The flow, in being lifted over the plume, is accelerated and deflected back toward the injector plate, tending to hold the plume close to it. An oblique recompression shock results in turning the flow parallel with the plate once more.

The separated boundary layer, which must also go over the plume, becomes mixed with the main flow and injectant. There is a small region of back flow just downstream of the injection orifice followed by re-attachment and growth of the boundary layer. As can be expected, the separated flow consists largely of injectant gas. Mixing near the plate, in and near the boundary layer, is much slower than at the top of the plume.

At lower injection pressures, the injectant plume is entirely within the boundary layer and looks somewhat like an aggravated surface roughness. As the pressure is increased and the plume height, or penetration height, approaches the boundary layer depth, the relative effectiveness of injection in producing disturbances in the main flow per amount of injectant employed decreases. In the limit of very large pressure, the injectant acts merely as the exhaust of a convergent nozzle, and the jet reaction effect overrides the flow disturbance effects.

When the injectant enters the main stream through a point-like orifice, the resulting flow field is three-dimensional in character. The jet forces its way through the boundary layer and almost entirely remains above it. It expands into a plume which is semi-axisymmetric with the horizontal plane of symmetry, above which the plume remains, being above the boundary layer. Since, in this case, the plume has finite dimensions in all directions, the flow can go around it as well as over and through. As a result, the mixing of the injectant gas with the main stream gas is not quite so rapid as previously. As the injectant goes through the boundary layer, it drags much of the low-energy air with it, particularly from the area behind the jet. This aspiration effect, along with the result of the flow's going around the plume on each side and the top, creates a pair of vortices much like wing-tip vortices in reverse. These vortices tend to contain the plume on top, but help to mix main stream gas into it from the sides and bottom. The effect is a somewhat mushroom-shaped cross section.

Because the boundary layer is able to go around and under the jet plume in this case, the separated flow behind the jet is largely main flow gas. Re-attachment of the boundary layer occurs fairly close behind the jet and it quickly reaches its former depth.

REFERENCES

1. Newton, J. F., Jr. and Spaid, F. W., "Interaction of Secondary Injectants and Rocket Exhaust for Thrust Vector Control," ARS Journal, Volume 32, No. 8 (August 1962), pp. 1203-1211.

2. Walker, R. E., Stone, A. R., and Shandor, M., "Secondary Gas Injection in a Conical Rocket Nozzle," AIAA Journal, Vol. 1, No. 2 (February 1963), pp. 334-338.

3. Green, C. J. and McCulloigh, F., Jr., "Liquid Injection Thrust Vector Control," AIAA Journal, Vol. 1, No. 3 (March 1963), pp. 573-578.

4. Broadwell, J. E., "Analysis of the Fluid Mechanics of Secondary Injection for Thrust Vector Control," AIAA Journal, Volume 1, No. 5 (May 1963), pp. 1067-1075.

5. Cubbison, R. W., Anderson, B. H., and Ward, J. J., "Surface Pressure Distributions with a Sonic Jet Normal to Adjacent Flat Surfaces at Mach 2.92 to 6.4," NASA TN D-580, Washington, D. C. (1951).

6. Zukoski, E. E. and Spaid, F. W., "Secondary Injection of Gases into a Supersonic Flow," Jet Propulsion Center, California Institute of Technology, Pasadena (1963).

7. Charwat, A., paper to be published in the AIAA Journal.

8. Puckett, A. E., "Final Report, Model Supersonic Wind Tunnel Project," GALCIT Report No. 43, California Institute of Technology (1943).

9. Spaid, F. W., "A Study of Secondary Injection of Gases into a Supersonic Flow," Ph. D. Thesis, California Institute of Technology, Pasadena (1964).

10. Liepmann, H. W. and Roshko, A., Elements of Gasdynamics, John Wiley and Sons, Inc., New York (1957).

11. Dailey, C. L. and Wood, L. C., Computation Curves for Compressible Fluid Problems, John Wiley and Sons, Inc., New York (1949).

12. Ames Research Center Staff, "Equations, Tables, and Charts for Compressible Flow," NACA Report 1135, Washington, D. C. (1953).

13. Parkhurst, R. C., and Holder, D. W., Wind-Tunnel Techniques, Sir Isaac Pitman and Sons, Ltd., London (1952).

14. Heyser, A. and Maurer, F., "Experimental Investigation on Solid Spoilers and Jet Spoilers at Mach Numbers of 0.6 to 2.8," Astronautics Information Translation No. 32, Jet Propulsion Laboratory, Pasadena, California (Feb. 21, 1964).

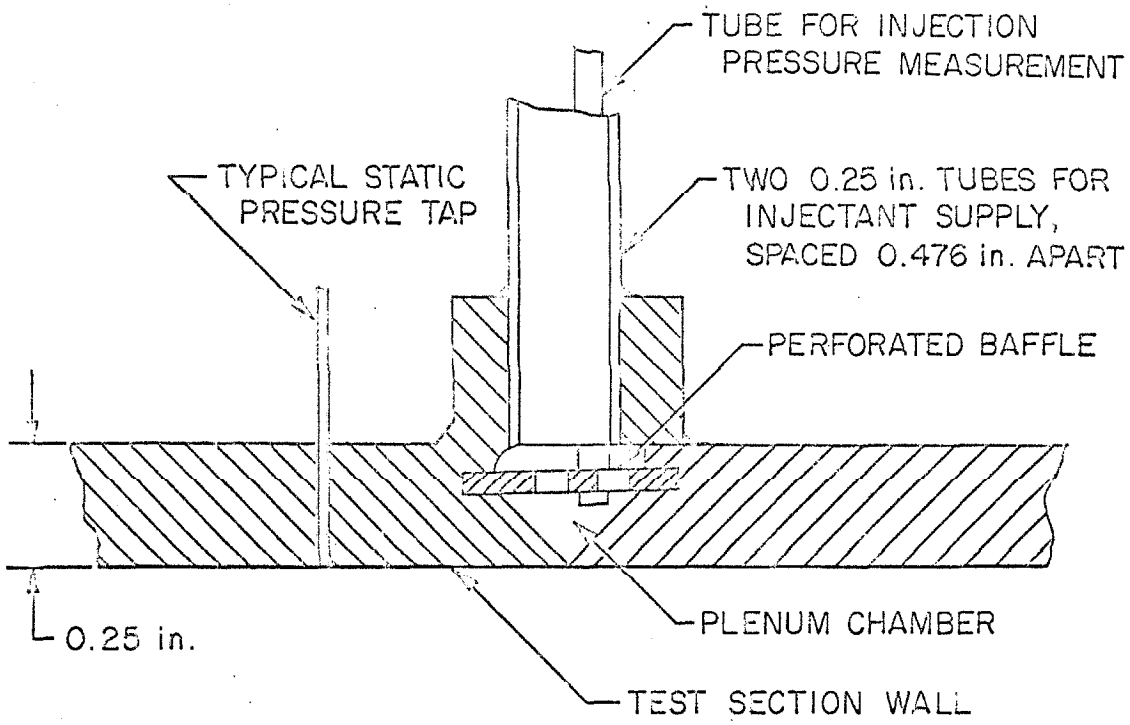

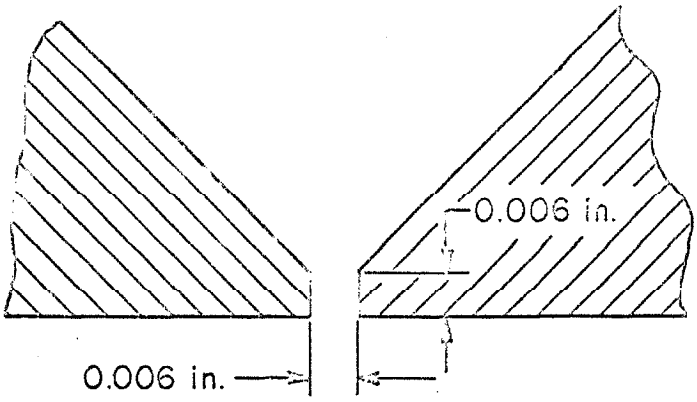

SLOT DETAIL

Fig. 1. Construction of Injector Used in Two-Dimensional Injection Experiment.

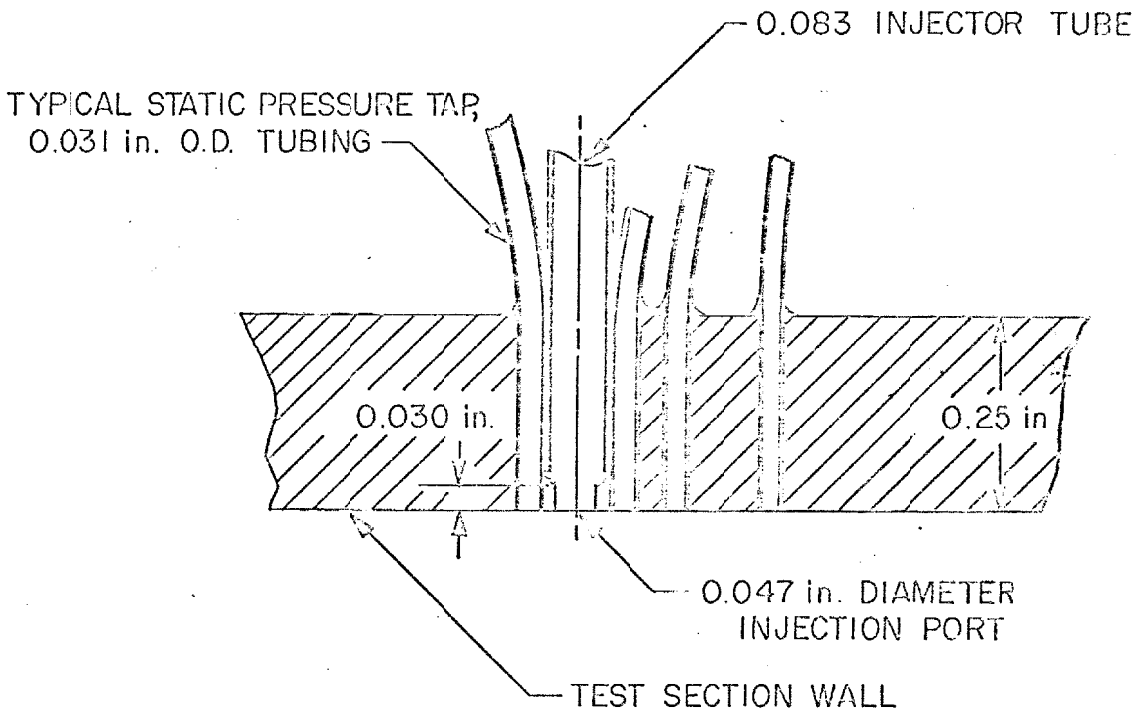

Fig. 2. Construction of Injector Used in Three-Dimensional Injection Experiment.

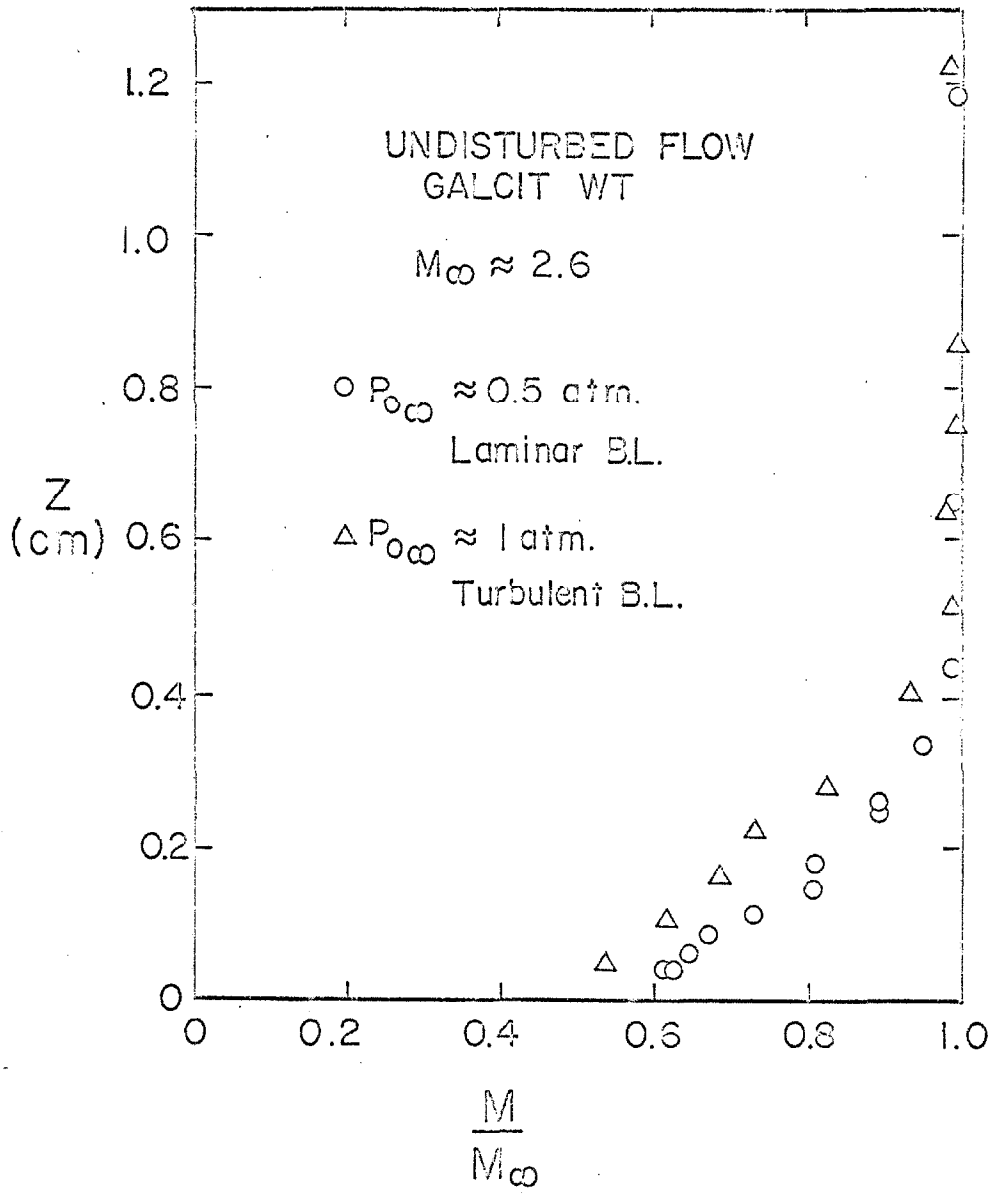

Fig. 3. Undisturbed Flow Mach-Number Profiles for Turbulent and Laminar Boundary Layers.

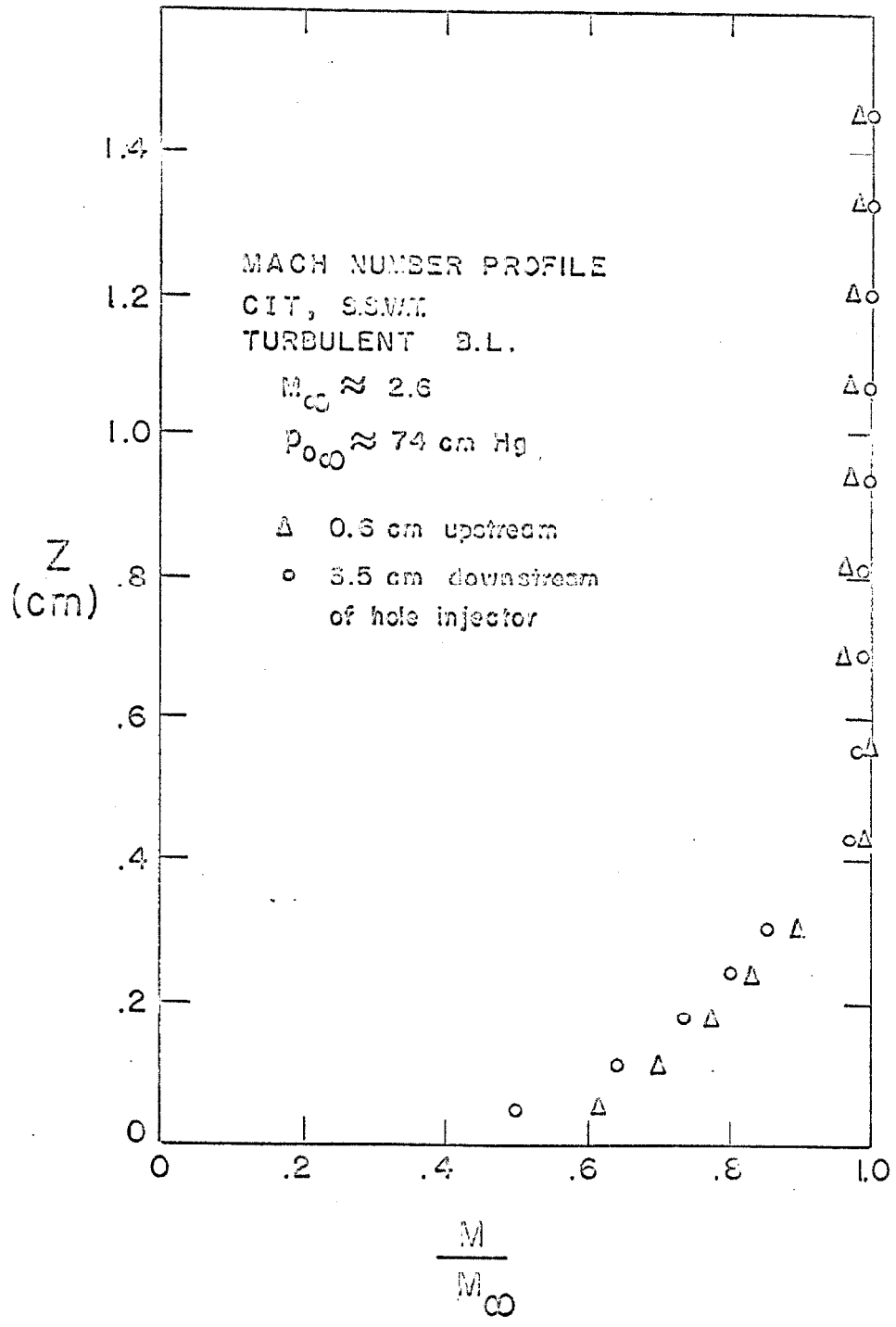

Fig. 4. Undisturbed Flow Mach-Number Profiles for Stations Upstream and Downstream of Injector Orifice.

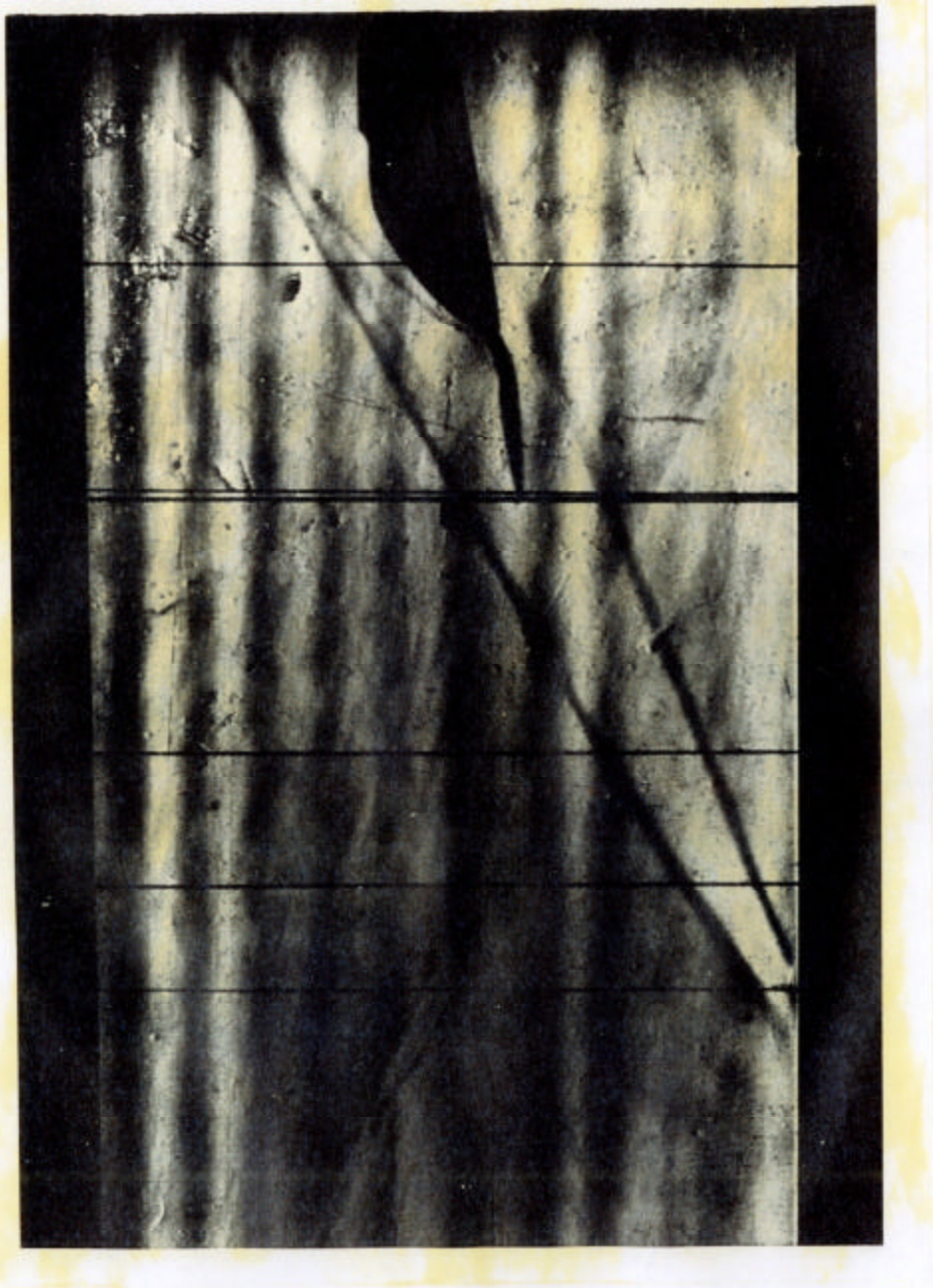

Fig. 5. Schlieren Picture of Flow Field with Two-Dimensional Injection and a Turbulent Boundary Layer. $M_\infty = 2.576$, $p_{0j}/p_{0\infty} = 1.6016$.

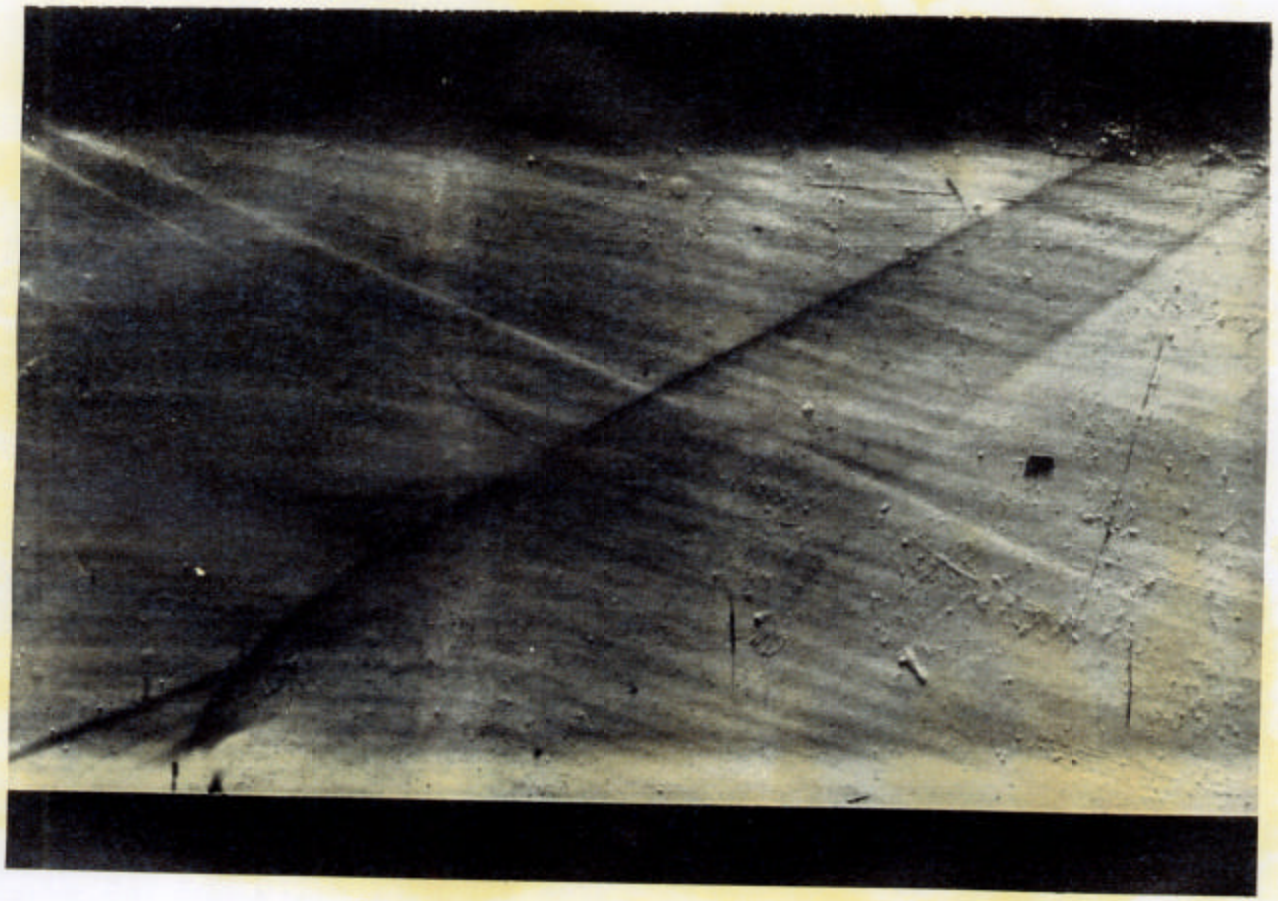

Fig. 6. Schlieren Picture of Flow Field with Three-Dimensional Injection and a Turbulent Boundary Layer. $M_\infty = 2.610$, $P_{0_j}/P_{0_\infty} = 7.77$.

Fig. 7. Schlieren Picture of Flow Field with Three-Dimensional Injection and a Laminar Boundary Layer. $M_\infty = 2.610$, $P_{0_j}/P_{0_\infty} = 30.2$.

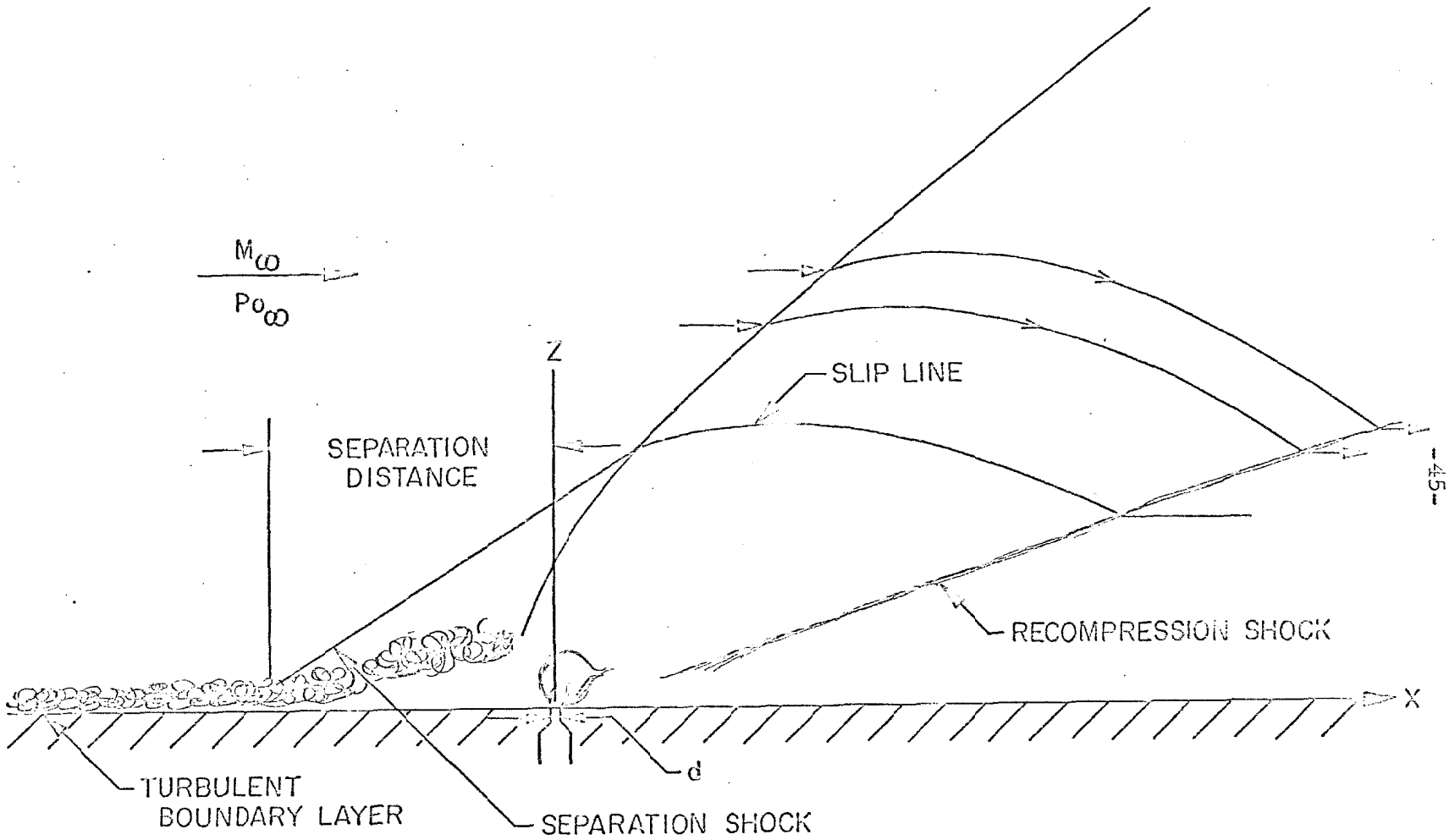

Fig. 8. Sketch of Flow Field with Two-Dimensional Injection and a Turbulent Boundary Layer.

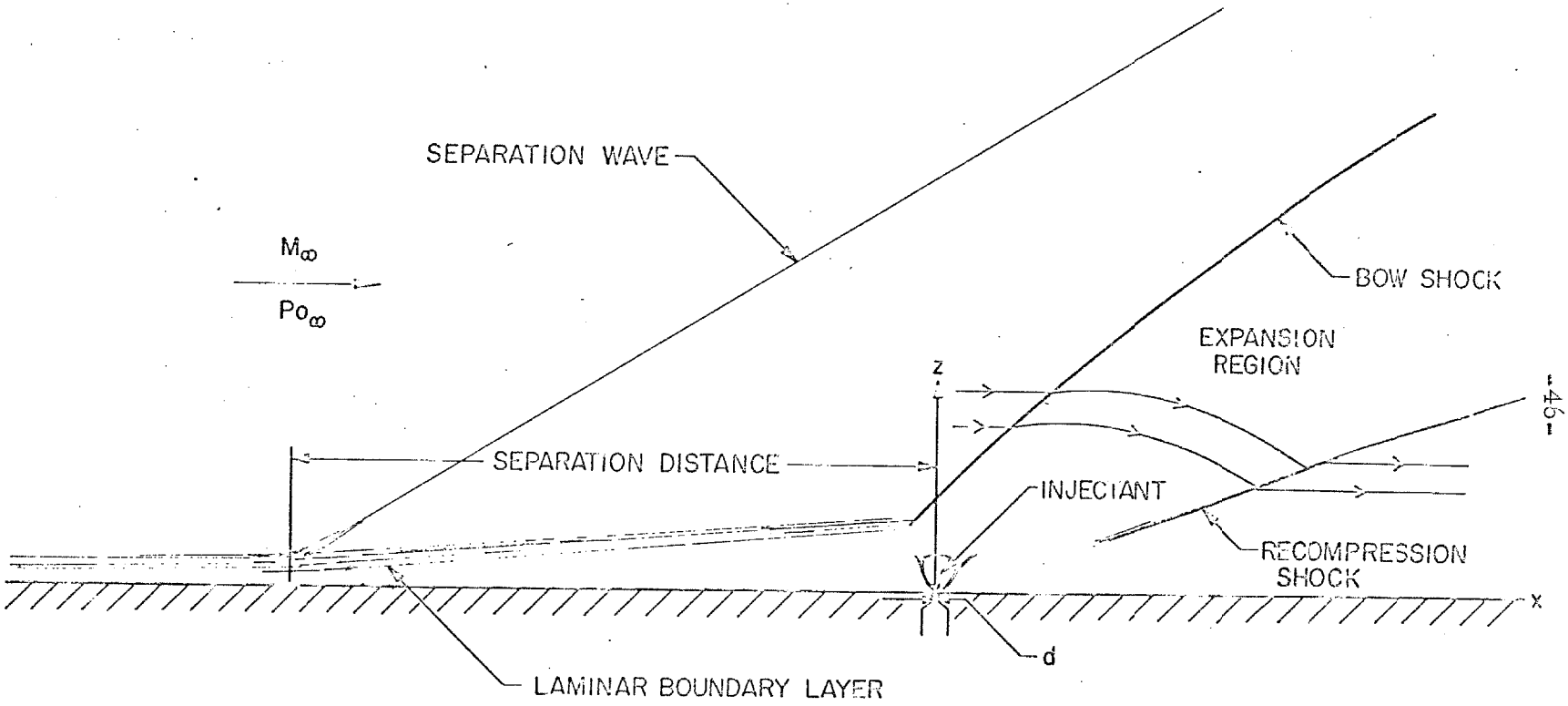

Fig. 9. Sketch of Flow Field with Two-Dimensional Injection and a Laminar Boundary Layer.

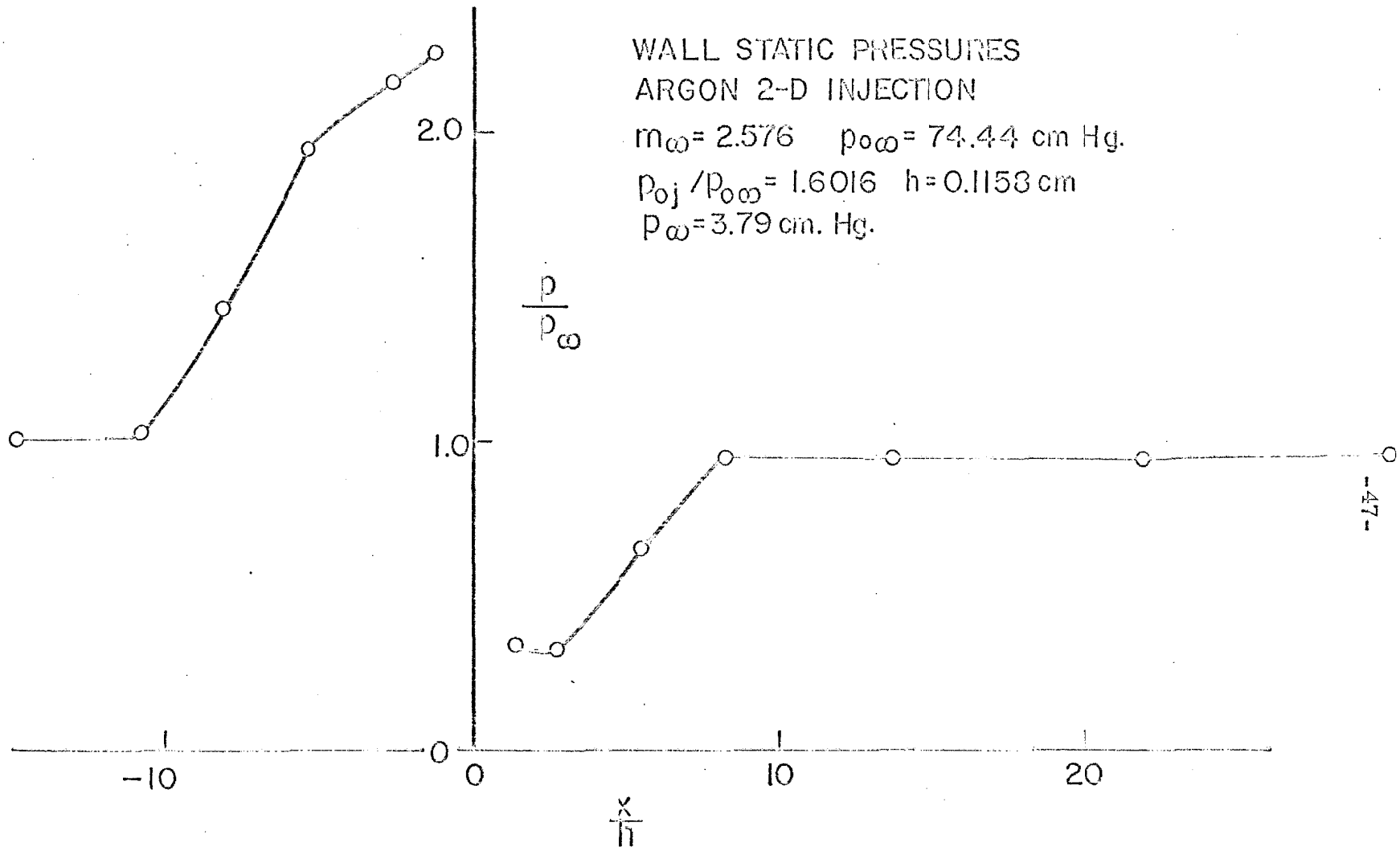

Fig. 10. Typical Wall Static Pressures During Two-Dimensional Injection with a Turbulent Boundary Layer.

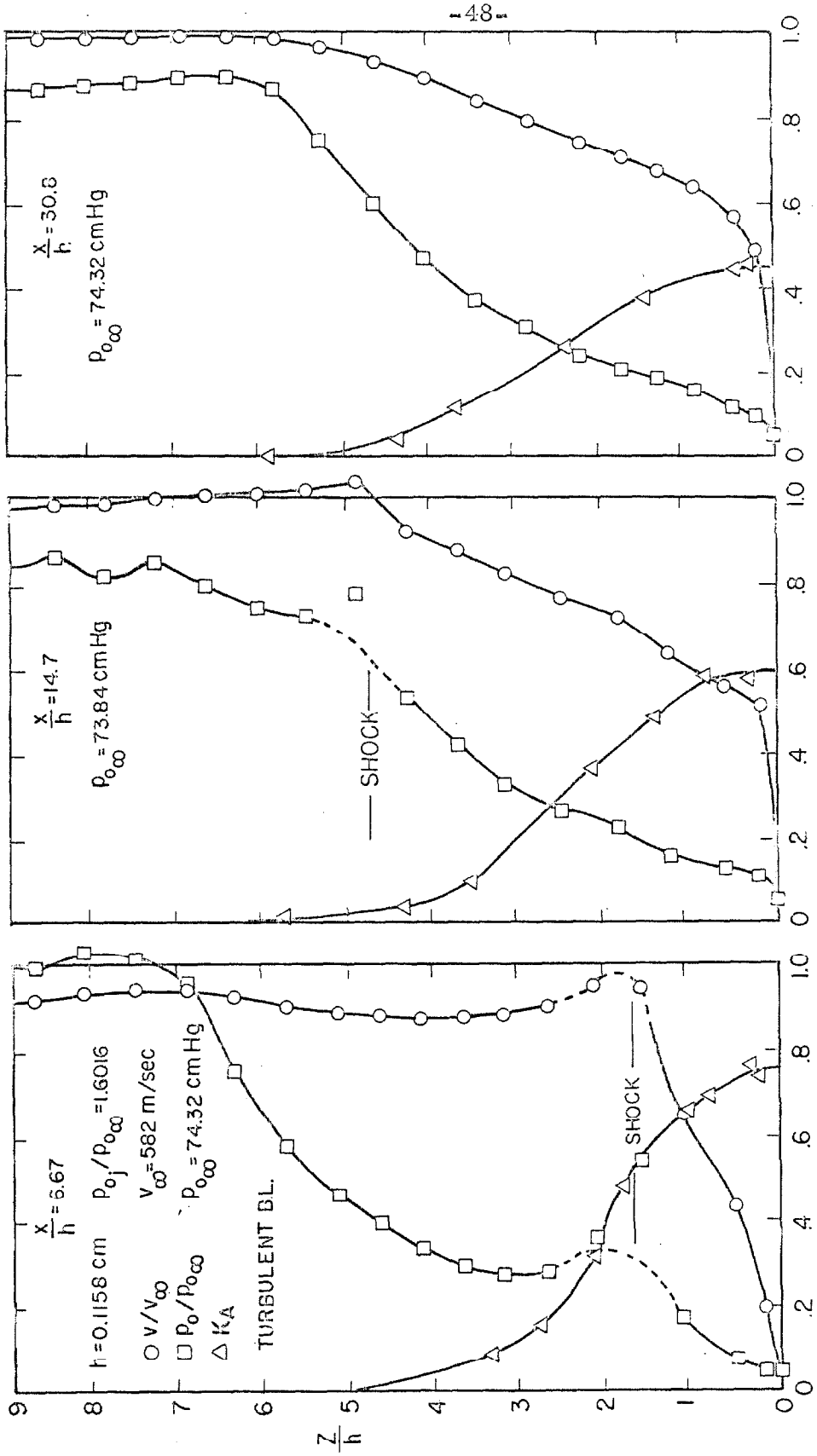

Fig. 11. Velocity Ratio, Total Pressure Ratio, and Concentration Profiles at Three Axial Stations for Two-Dimensional Injection of Argon with a Turbulent Boundary Layer. $M_\infty = 2.576$.

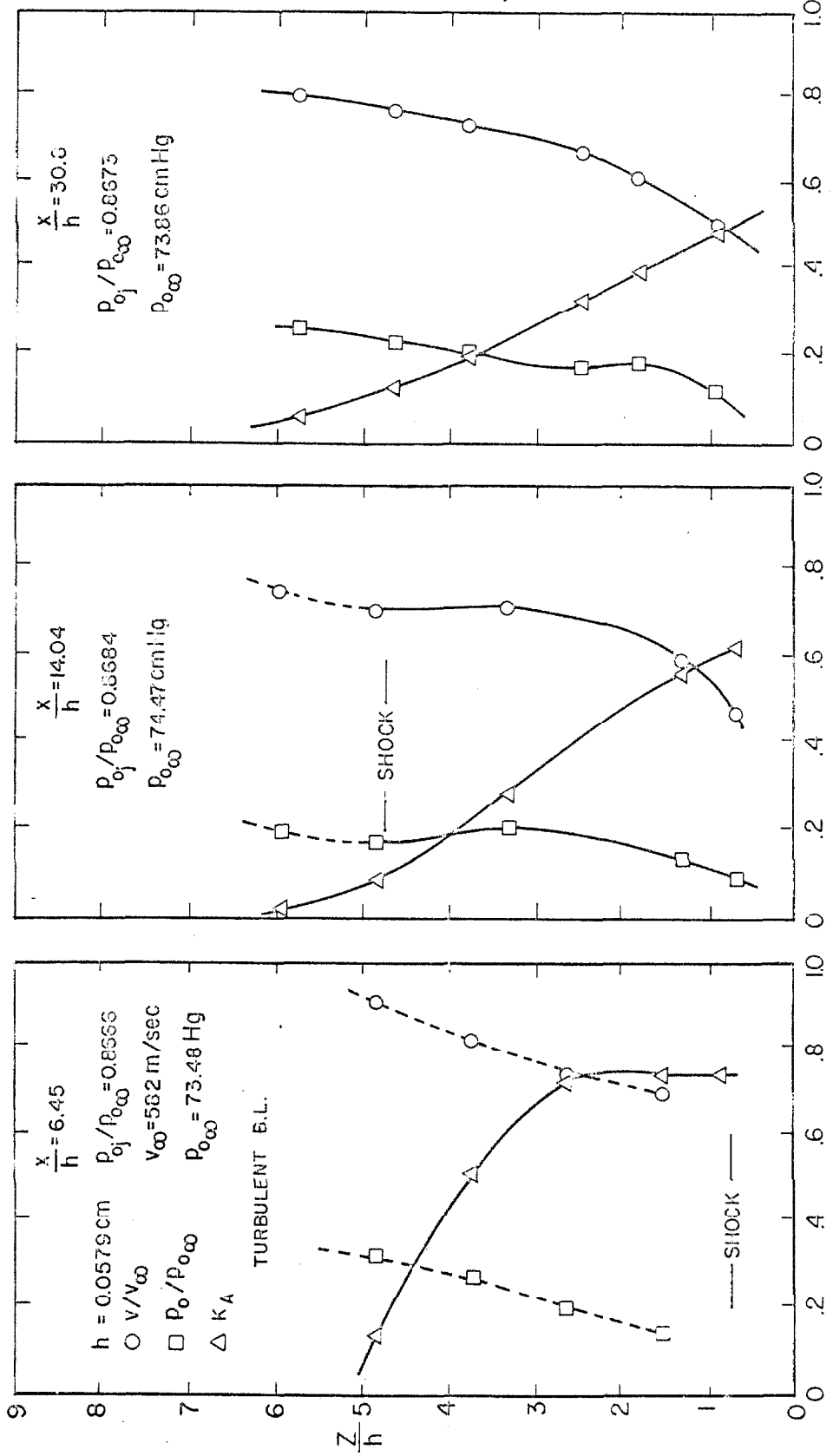

Fig. 12. Velocity Ratio, Total Pressure Ratio, and Concentration Profiles at Three Axial Stations for Two-Dimensional Injection of Argon with a Turbulent Boundary Layer. $M_\infty = 2.6$.

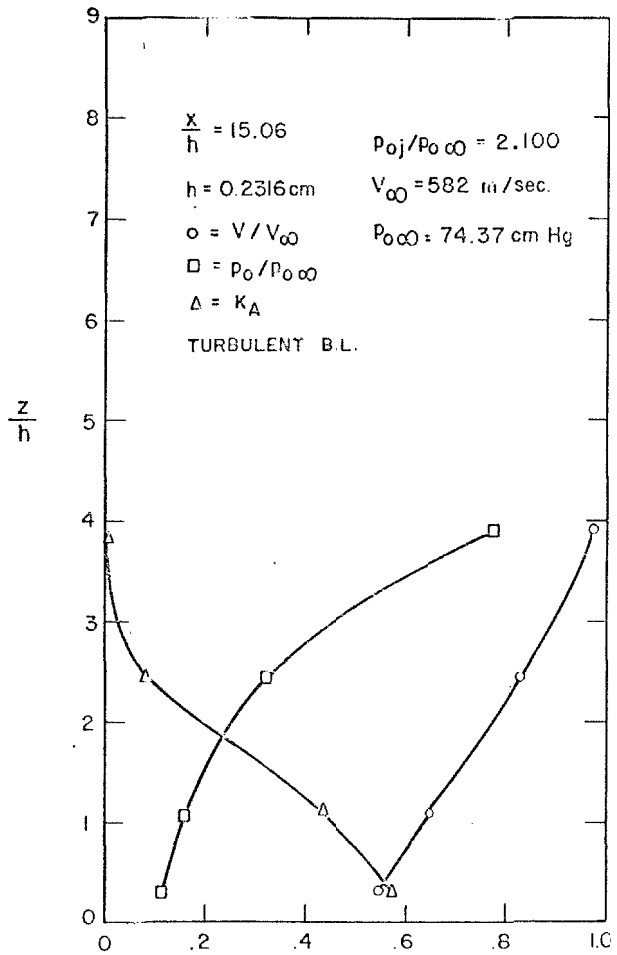

Fig. 13. Velocity Ratio, Total Pressure Ratio, and Concentration Profile at One Axial Station for Two-Dimensional Injection of Argon with a Turbulent Boundary Layer. $M_\infty = 2.6$.

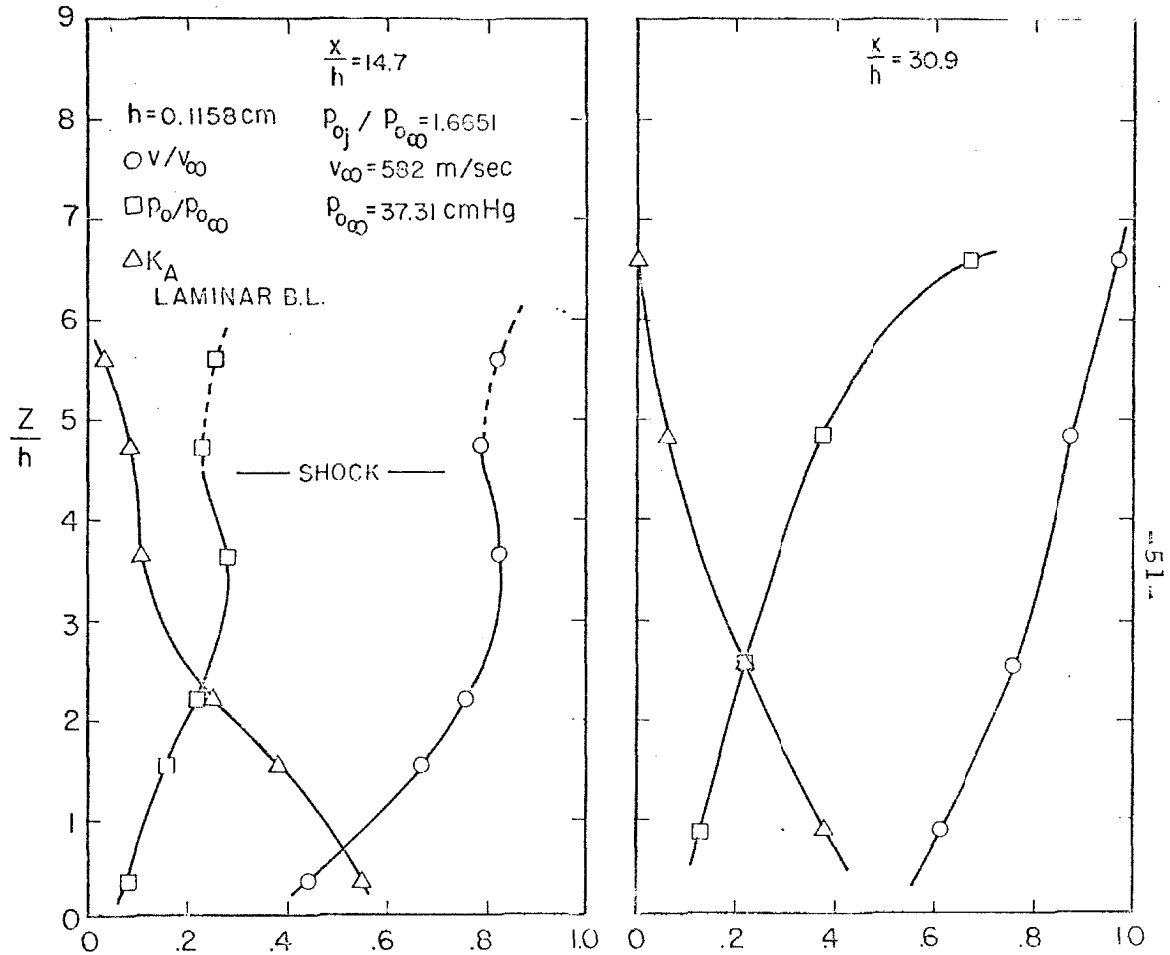

Fig. 14. Velocity Ratio, Total Pressure Ratio, and Concentration Profiles at Two Axial Stations for Two-Dimensional Injection of Argon with a Laminar Boundary Layer. $M_\infty = 2.6$.

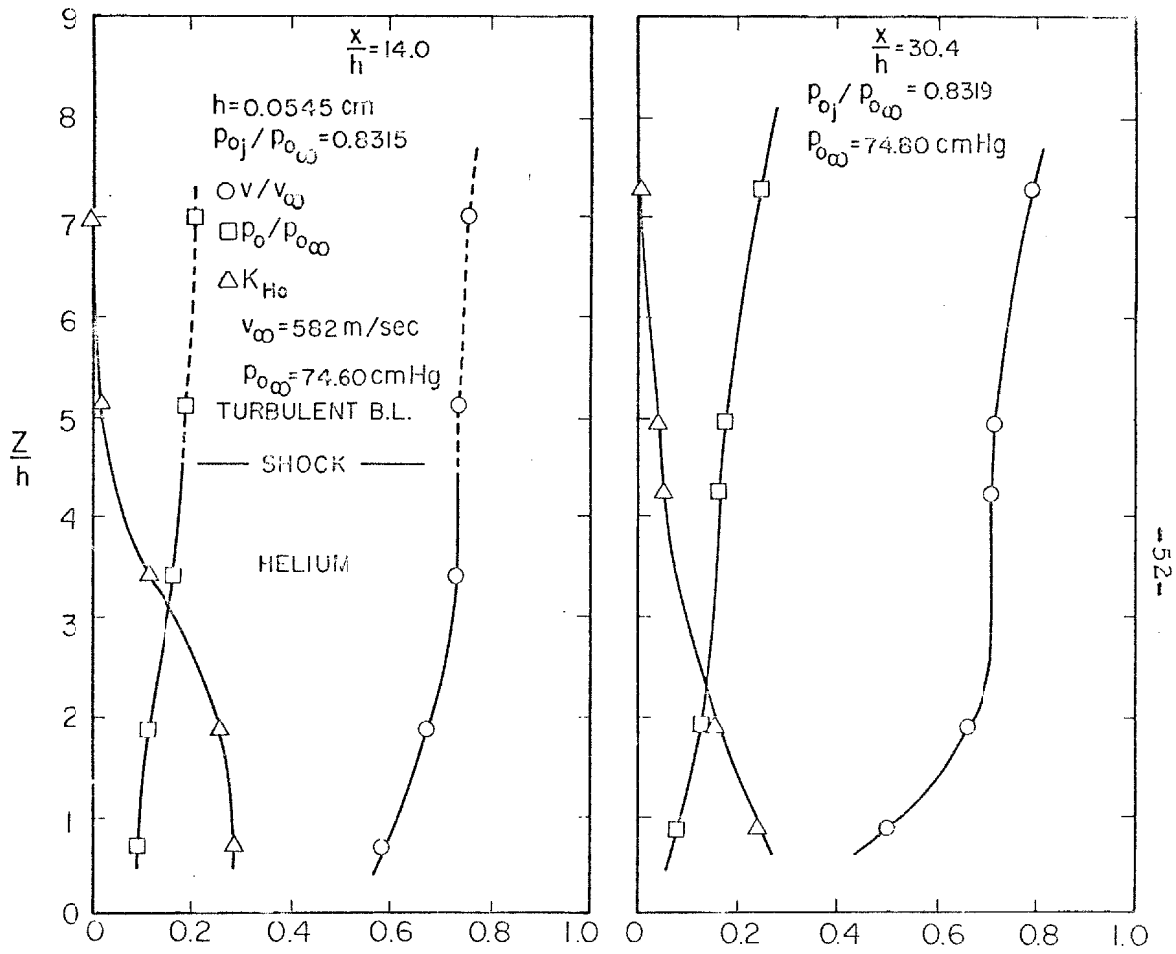

Fig. 15. Velocity Ratio, Total Pressure Ratio, and Concentration Profiles at Two Axial Stations for Two-Dimensional Injection of Helium with a Turbulent Boundary Layer. $M_\infty = 2.6$.

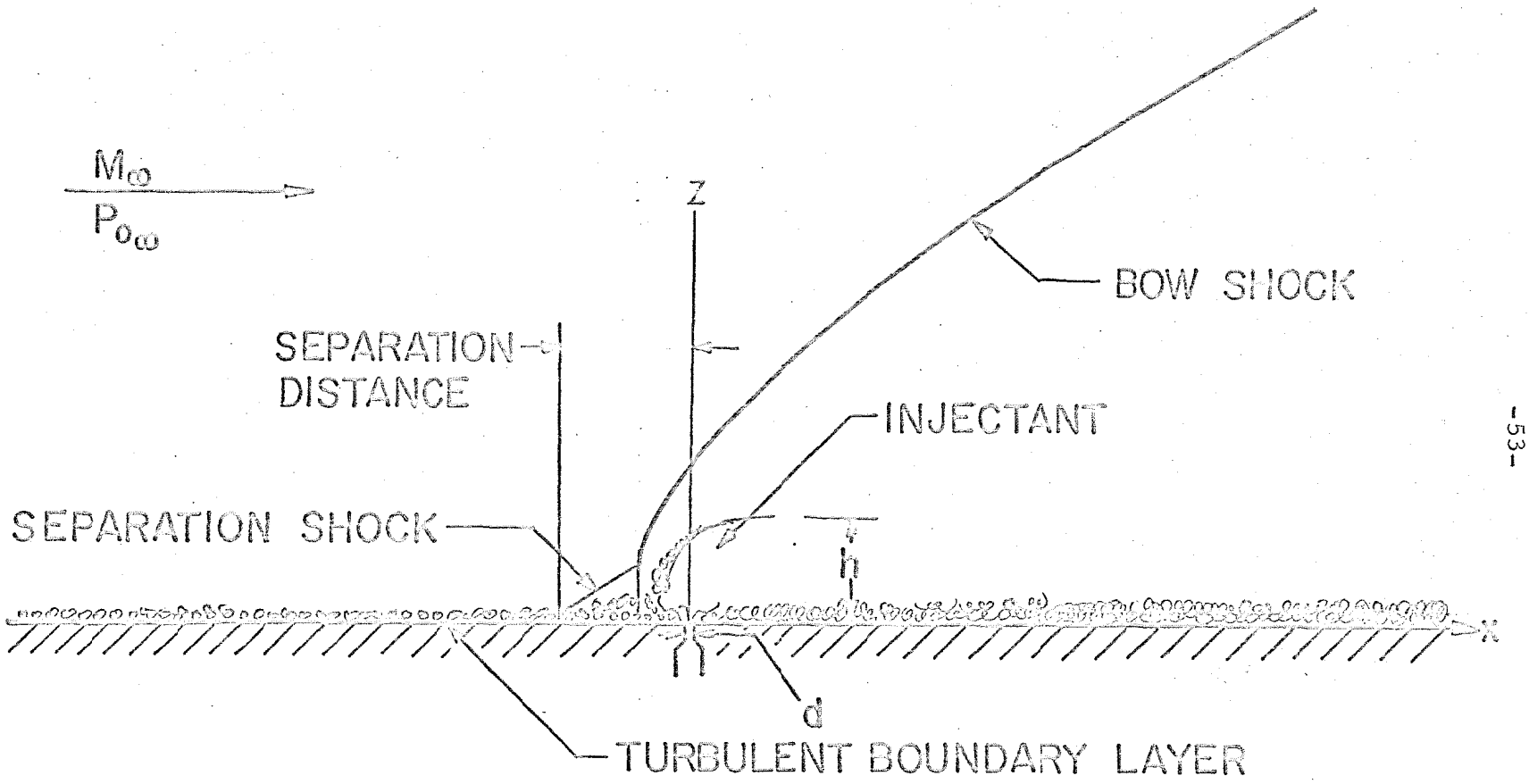

Fig. 16. Sketch of Flow Field with Three-Dimensional Injection and a Turbulent Boundary Layer.

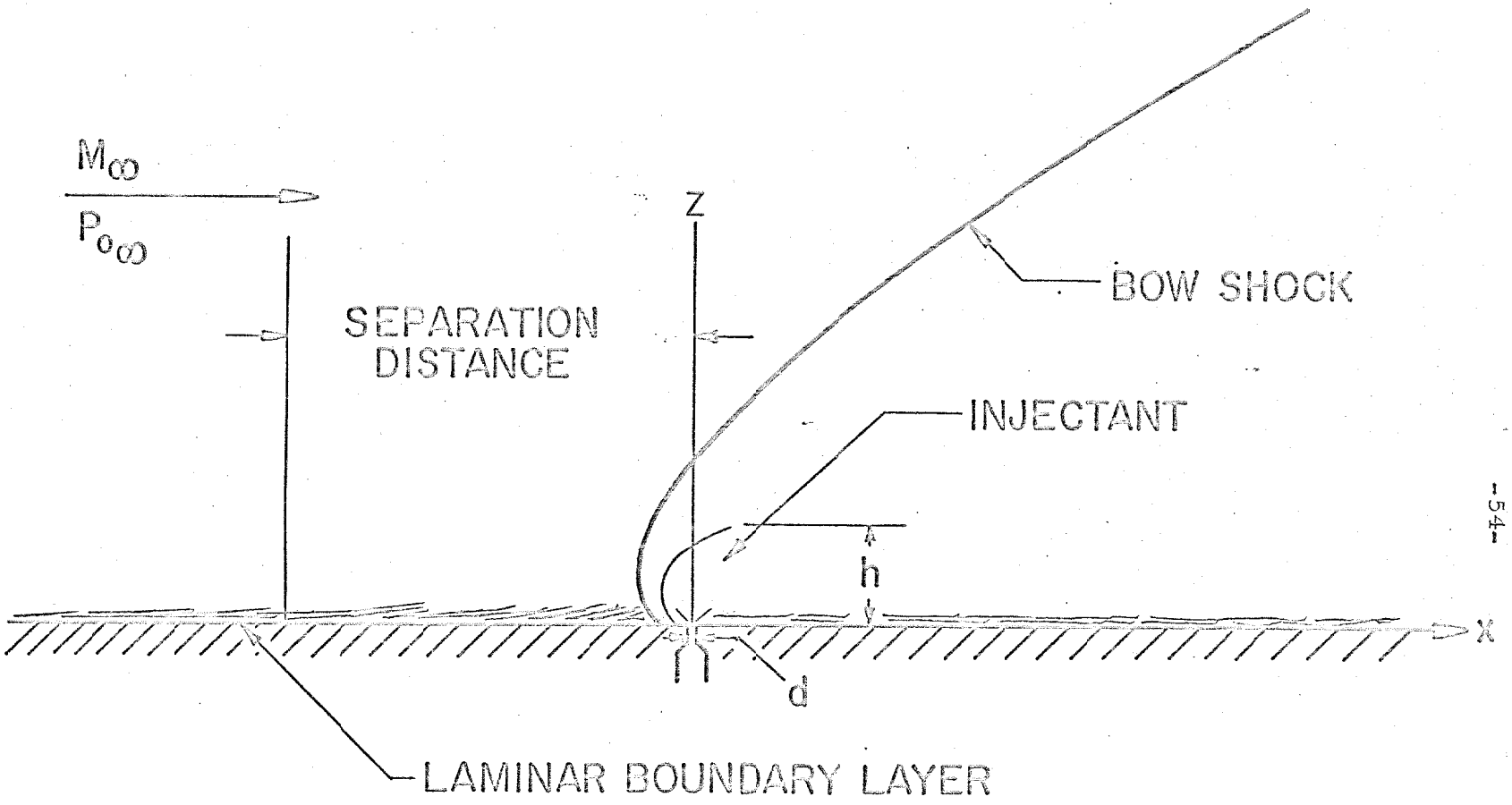

Fig. 17. Sketch of Flow Field with Three-Dimensional Injection and a Laminar Boundary Layer.

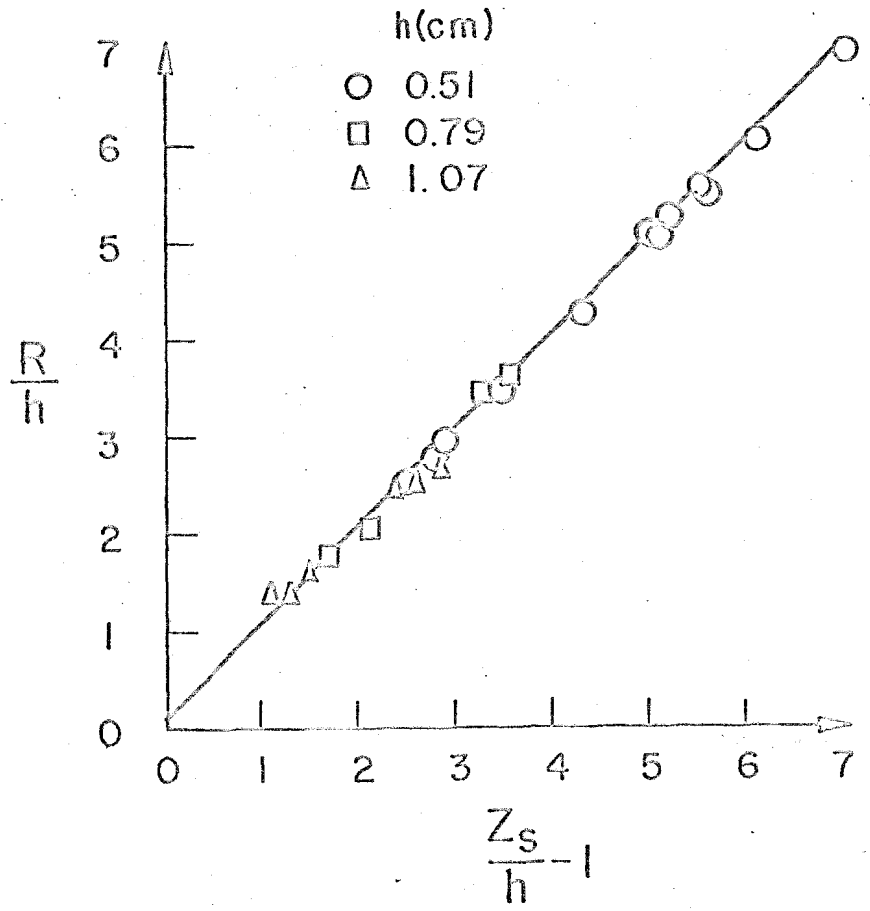

Fig. 18a. Linear Comparison of Normalized Dimensions of Shock Shapes Showing Axisymmetry of Shock with Three-Dimensional Injection. $M_\infty = 2.610$.

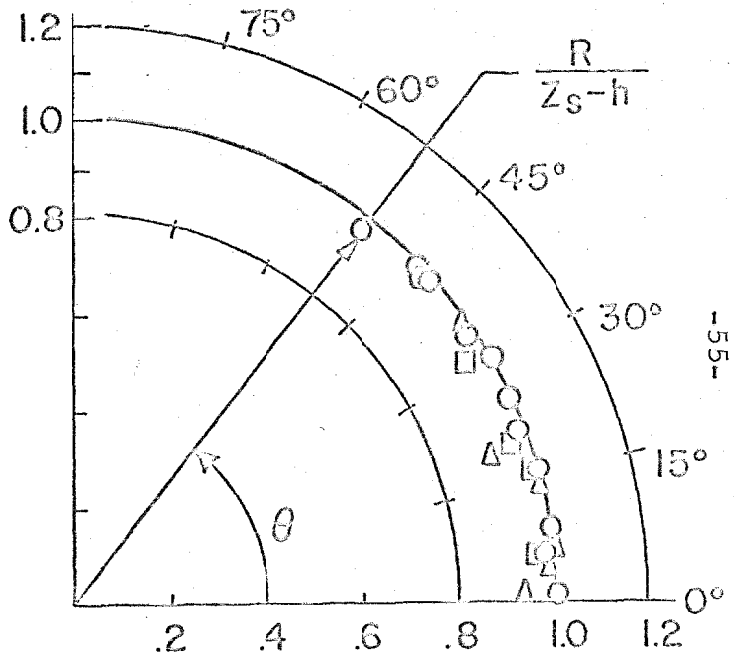

Fig. 18b. Polar Plot of Ratio of Normalized Shock Dimensions from Figure 18a as Functions of Position in Injectant Plume Cross-Section.

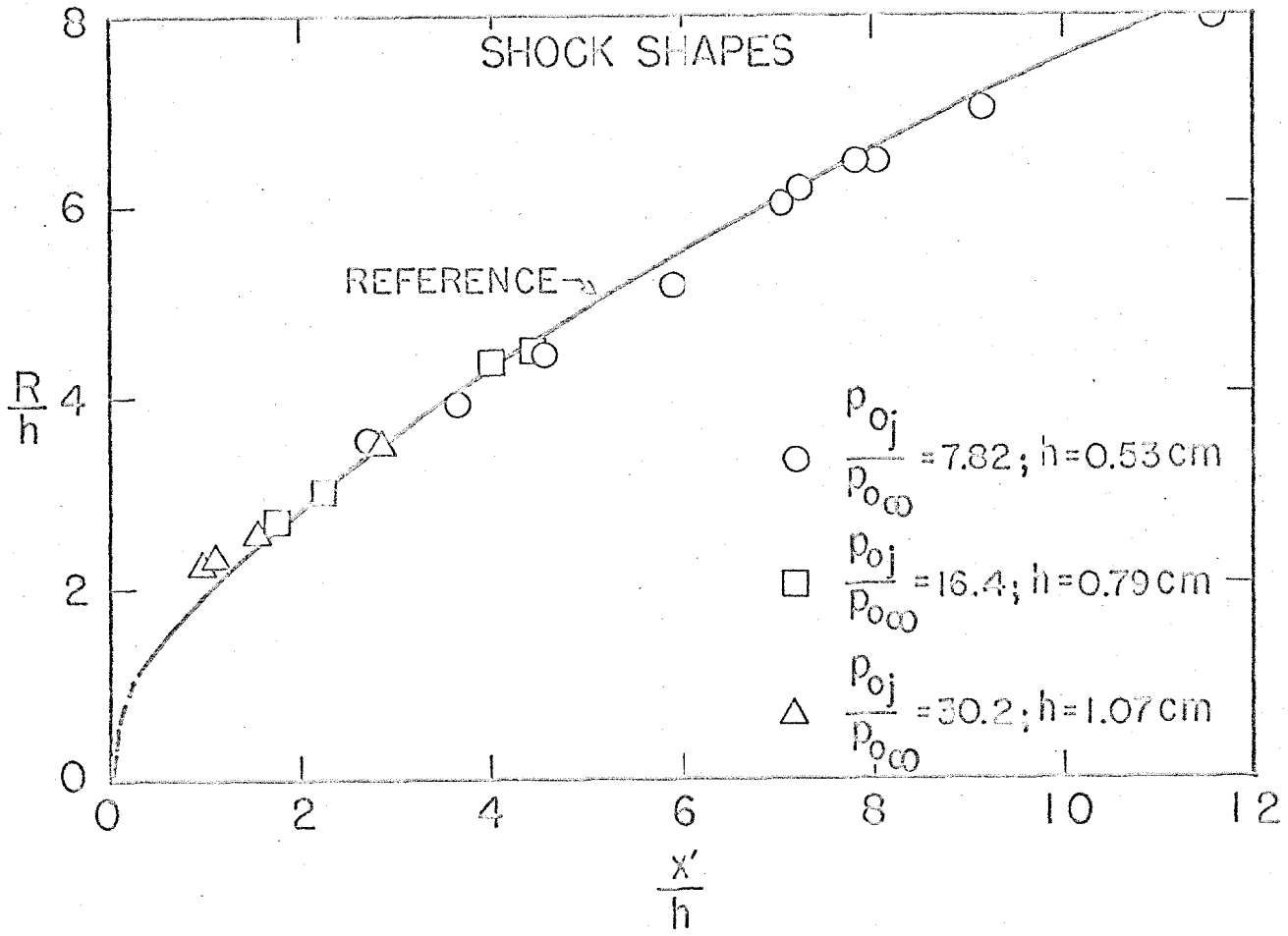

Fig. 19. Comparison of Off-Centerline Shock Radii with Centerline Shock Shapes Measured from Schlieren Pictures (Reference), $M_\infty = 2.610$.

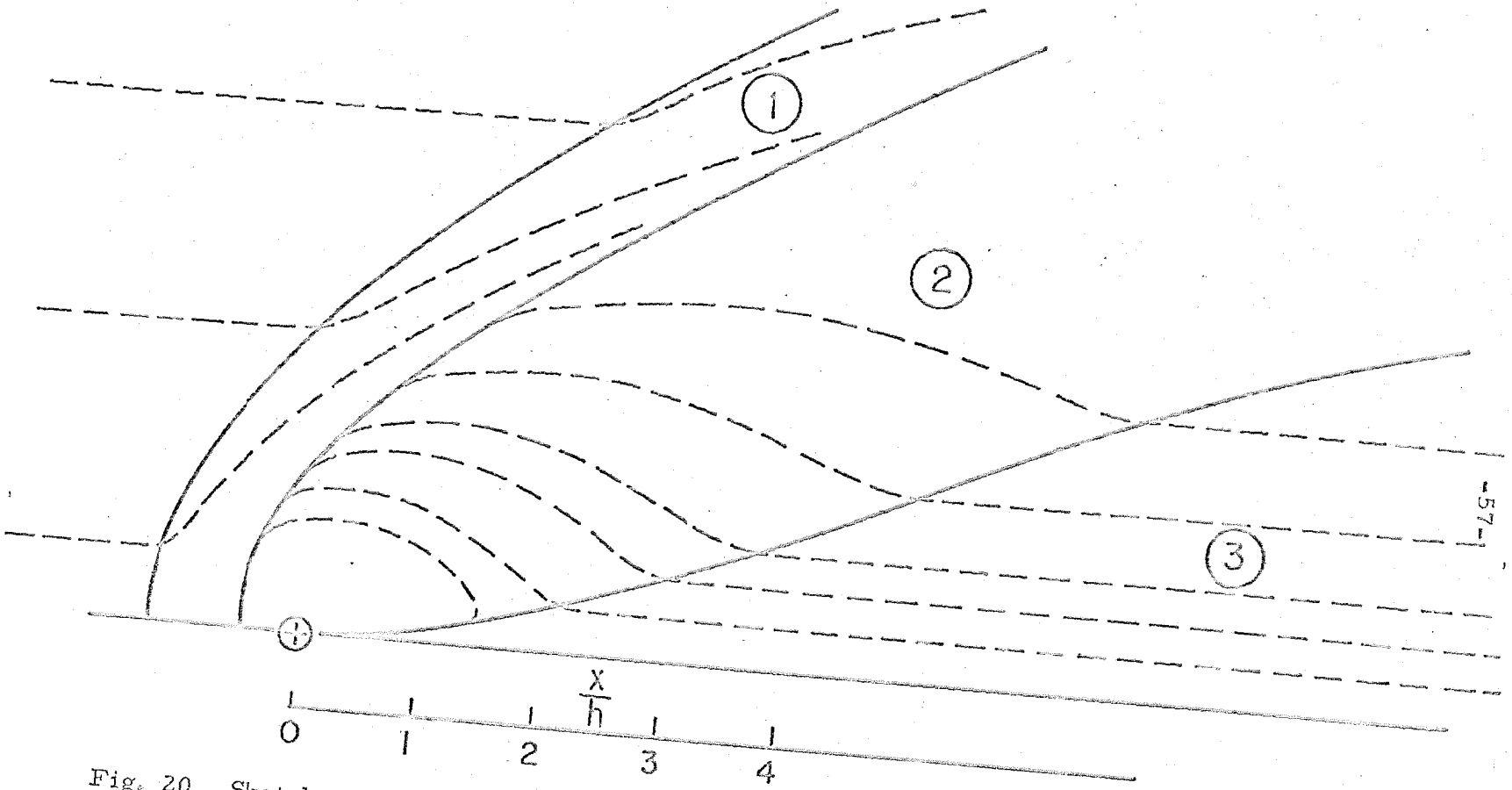

Fig. 20. Sketch of Flow Pattern in Boundary Layer During Three-Dimensional Injection at $P_{0_j}/P_{0_\infty} = 7.77$ and a Turbulent Boundary Layer. $M_\infty = 2.610$.

Fig. 21. Photograph of Injector Plate Showing Effect of Boundary Layer Flow upon Grease Mixture During Three-Dimensional Injection at $p_{0_j}/p_{0_\infty} = 7.77$ and a Turbulent Boundary Layer. $M_\infty = 2.610$.

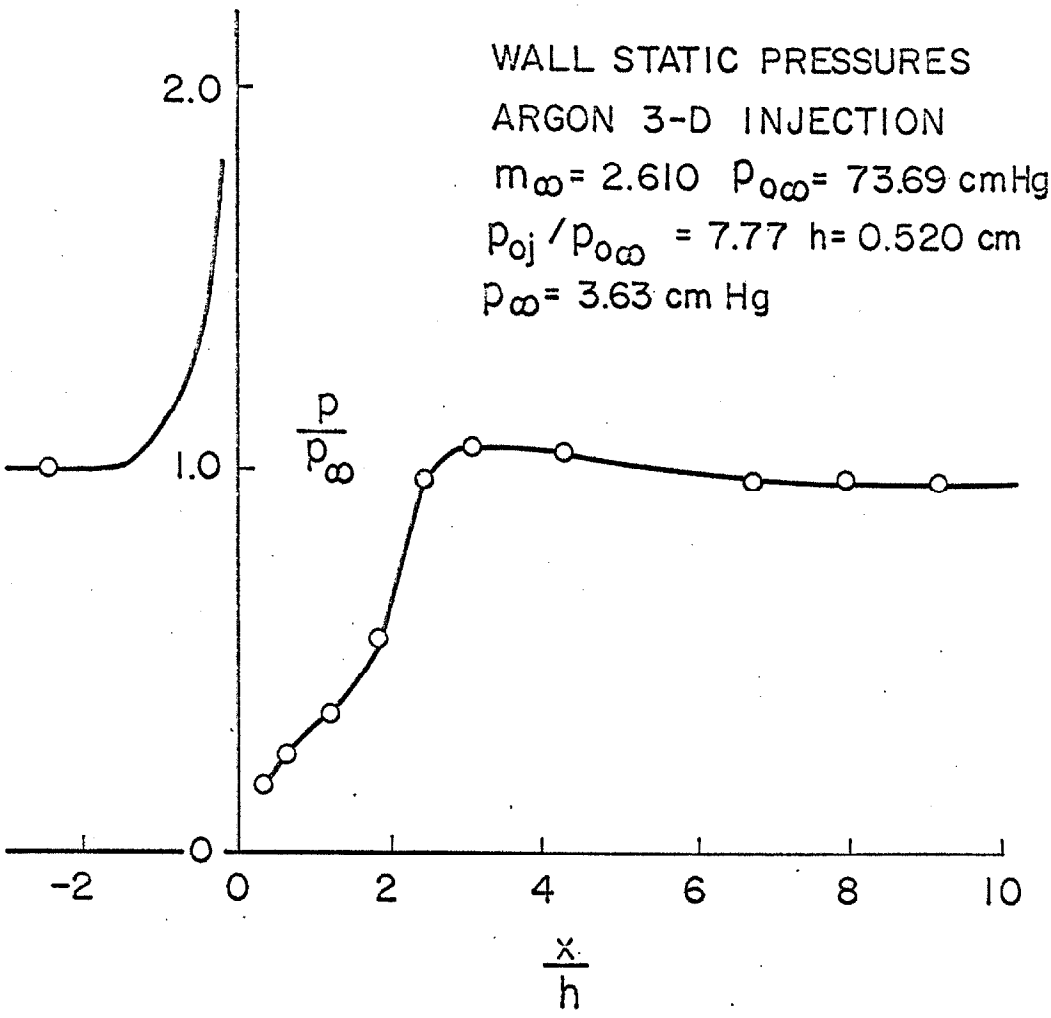

Fig. 22. Typical Wall Static Pressure During Three-Dimensional Injection with a Turbulent Boundary Layer.

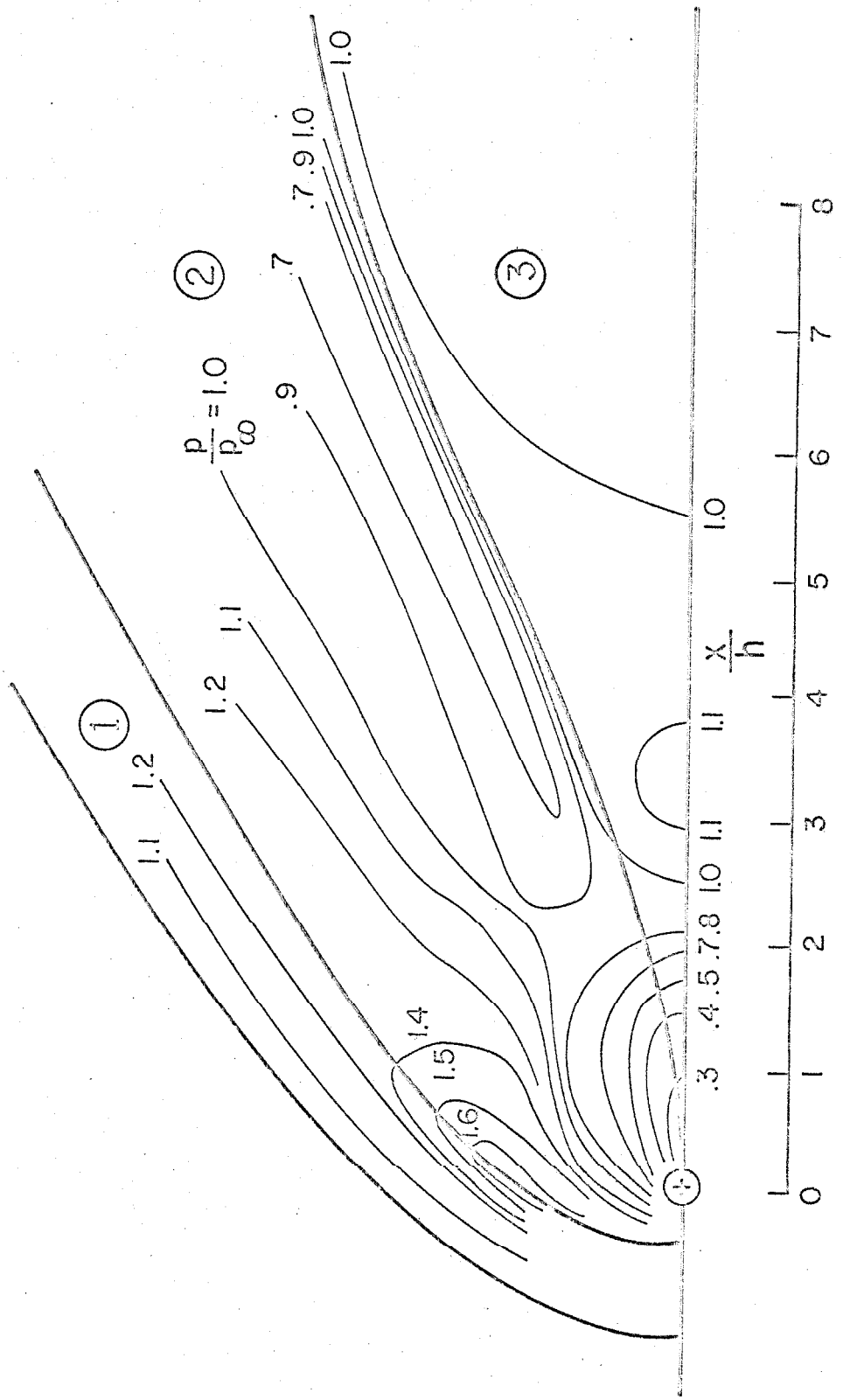

Fig. 23. Static Pressure Ratio (p/p_∞) Contours and Boundary Layer Flow Visualization Compared at P_{0_j}/P_{0_∞} = 7.77 and M_∞ = 2.610.

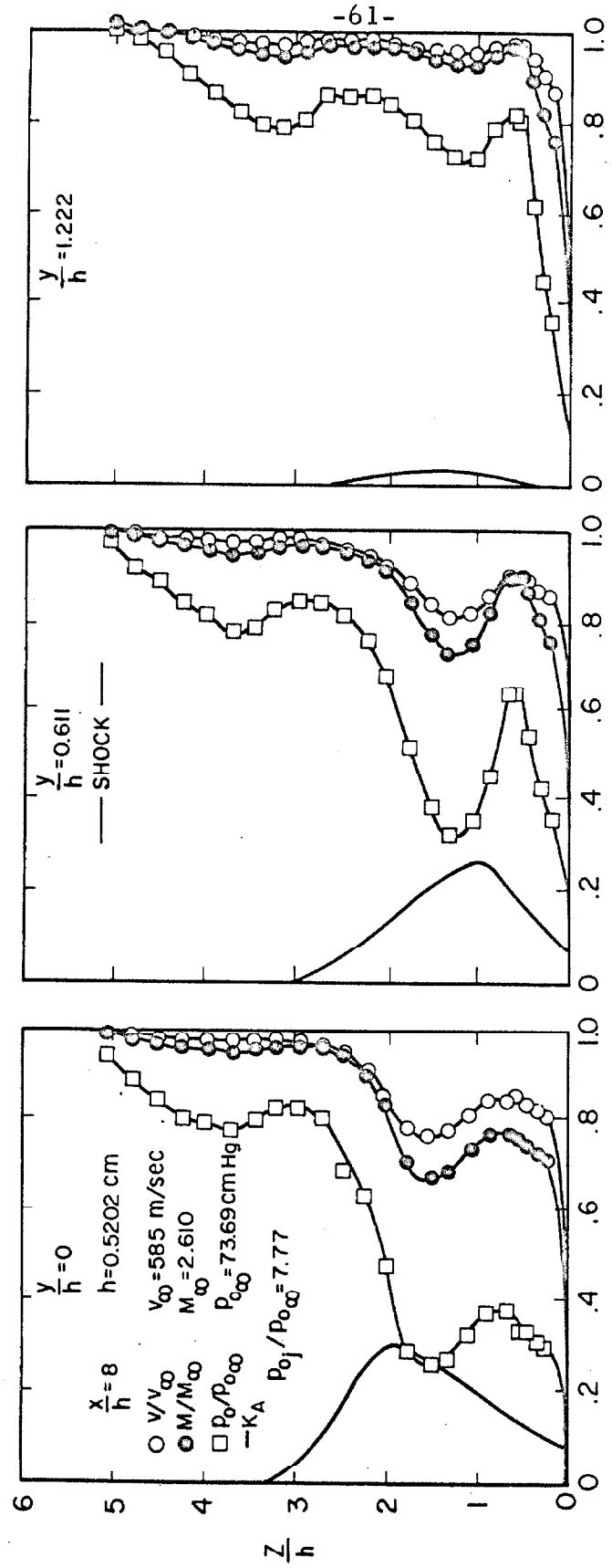

Fig. 24. Velocity Ratio, Total Pressure Ratio, Mach Number Ratio, and Concentration Profiles at Three Lateral Stations at x/h = 8 for Three-Dimensional Injection with a Turbulent Boundary Layer. $M_\infty = 2.610$.

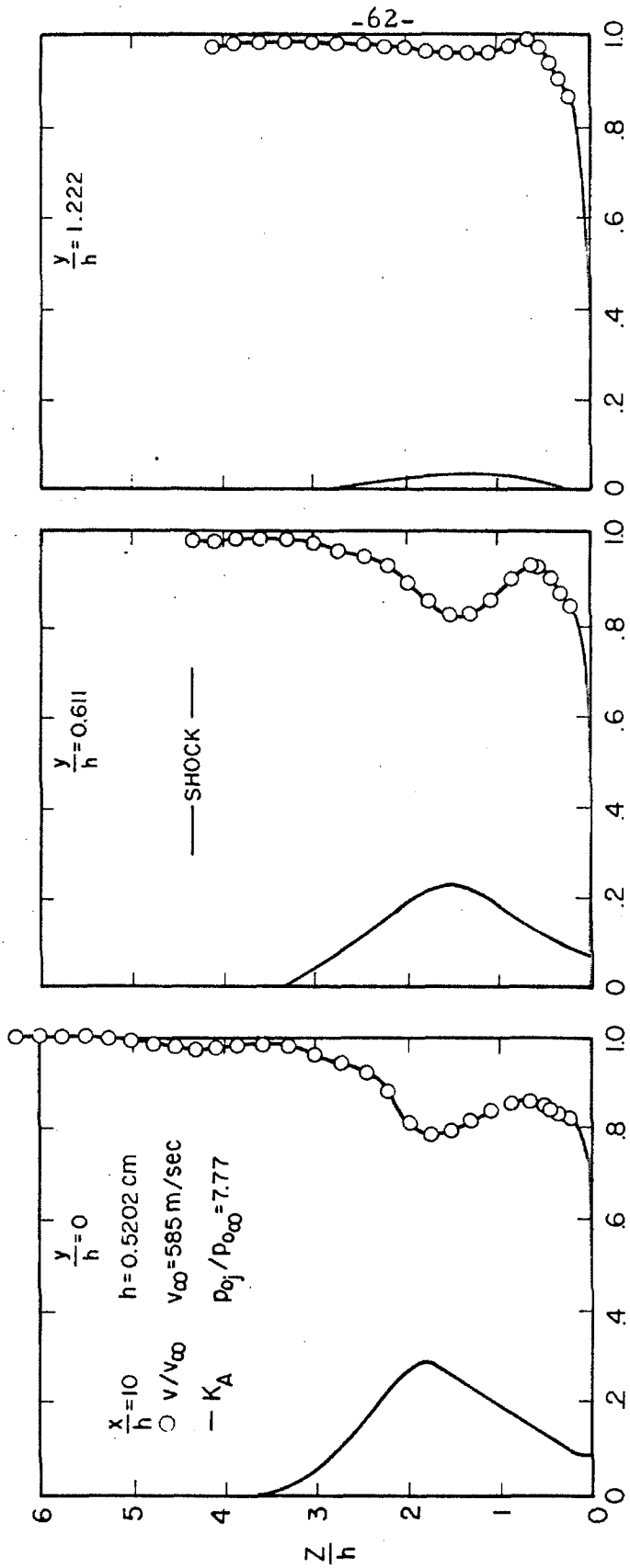

Fig. 25. Velocity Ratio and Concentration Profiles at Three Lateral Stations at x/h = 10 for Three-Dimensional Injection with a Turbulent Boundary Layer. M_∞ = 2.610.

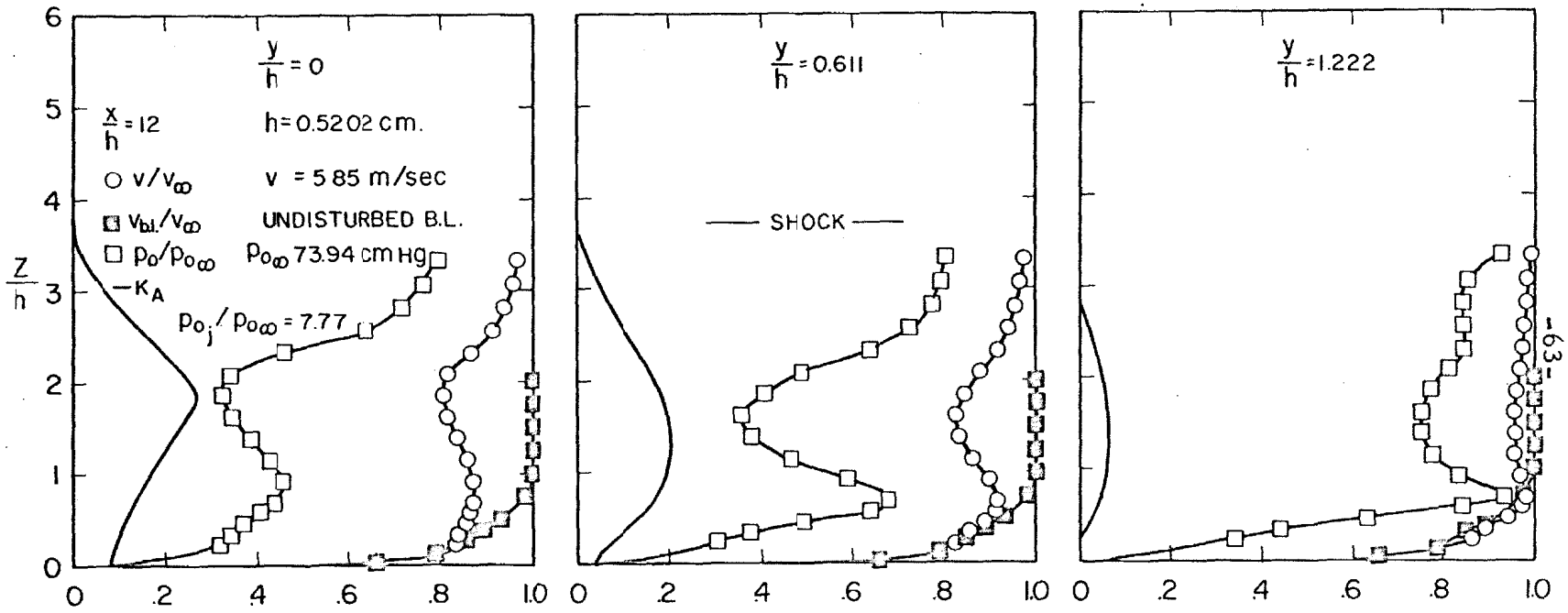

Fig. 26. Velocity Ratio, Undisturbed Boundary-Layer Velocity Ratio, Total Pressure Ratio, and Concentration Profiles at Three Lateral Stations at x/h = 12 for Three-Dimensional Injection with a Turbulent Boundary Layer. $M_\infty = 2.610$.

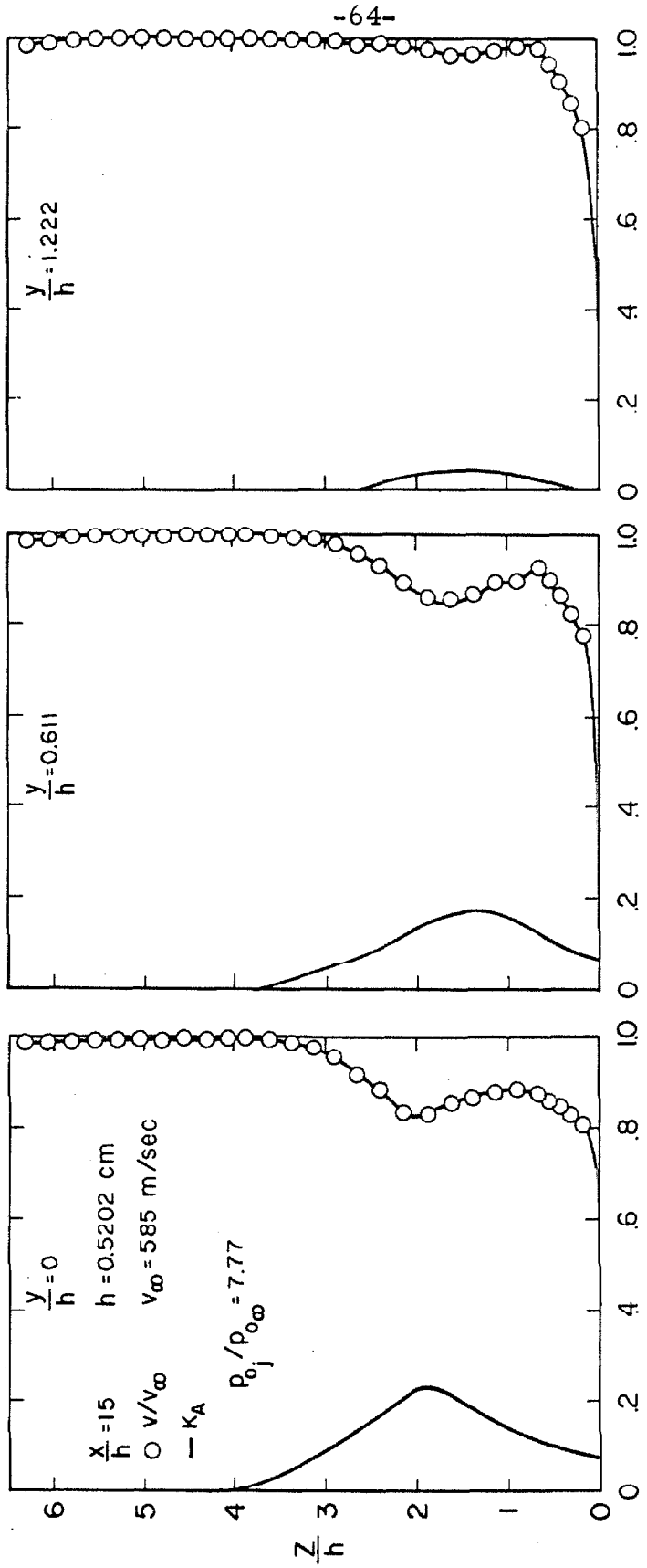

Fig. 27. Velocity Ratio and Concentration Profiles at Three Lateral Stations at x/h = 15 for Three-Dimensional Injection with a Turbulent Boundary Layer. M_∞ = 2.610.

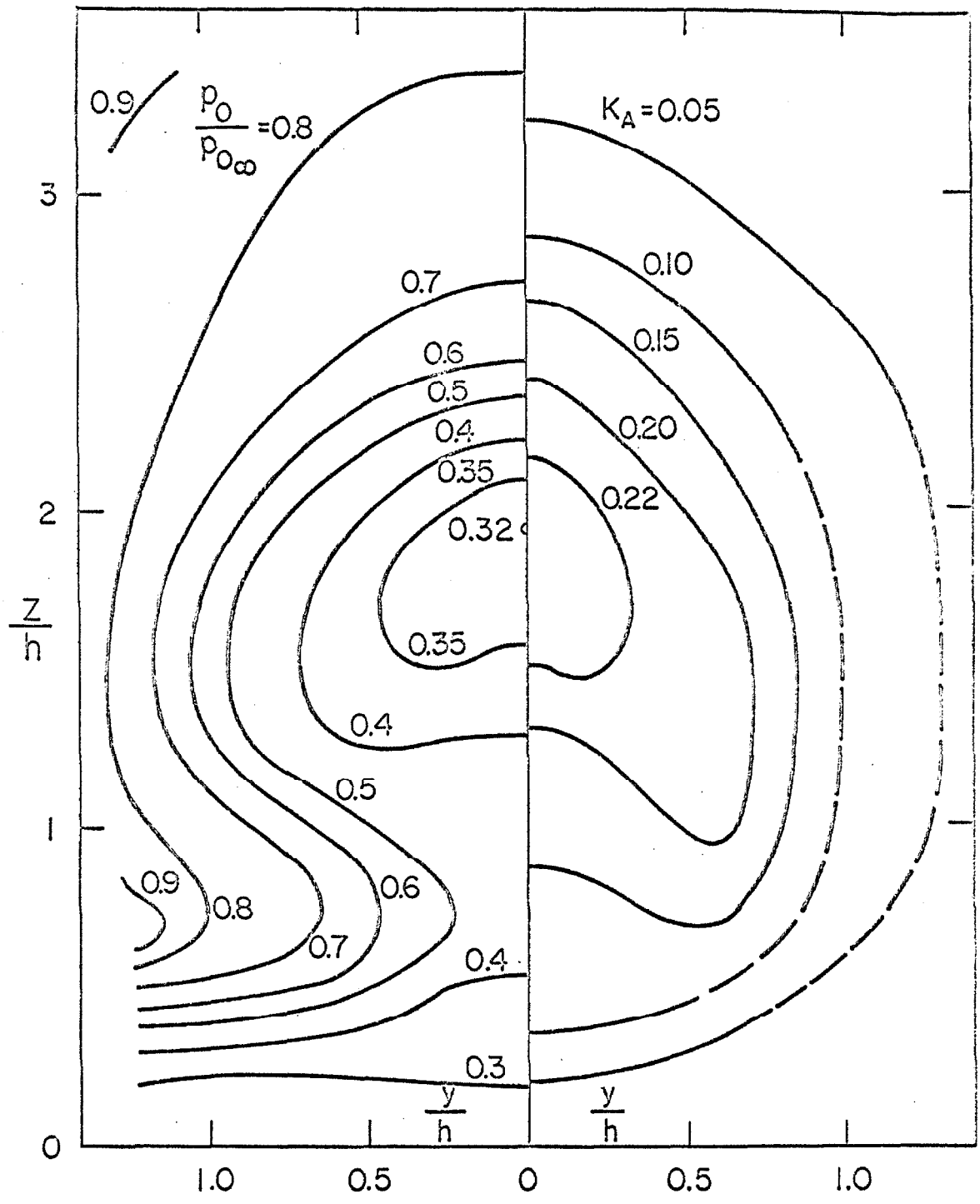

Fig. 28. Comparison of Total Pressure Ratio and Concentration Contours at $x/h \approx 12$, $M_\infty \approx 2.6$, $p_{0_\infty} \approx 74$ cm Hg, $p_{0_j}/p_{0_\infty} = 7.77$, and $h = 0.52$ cm.

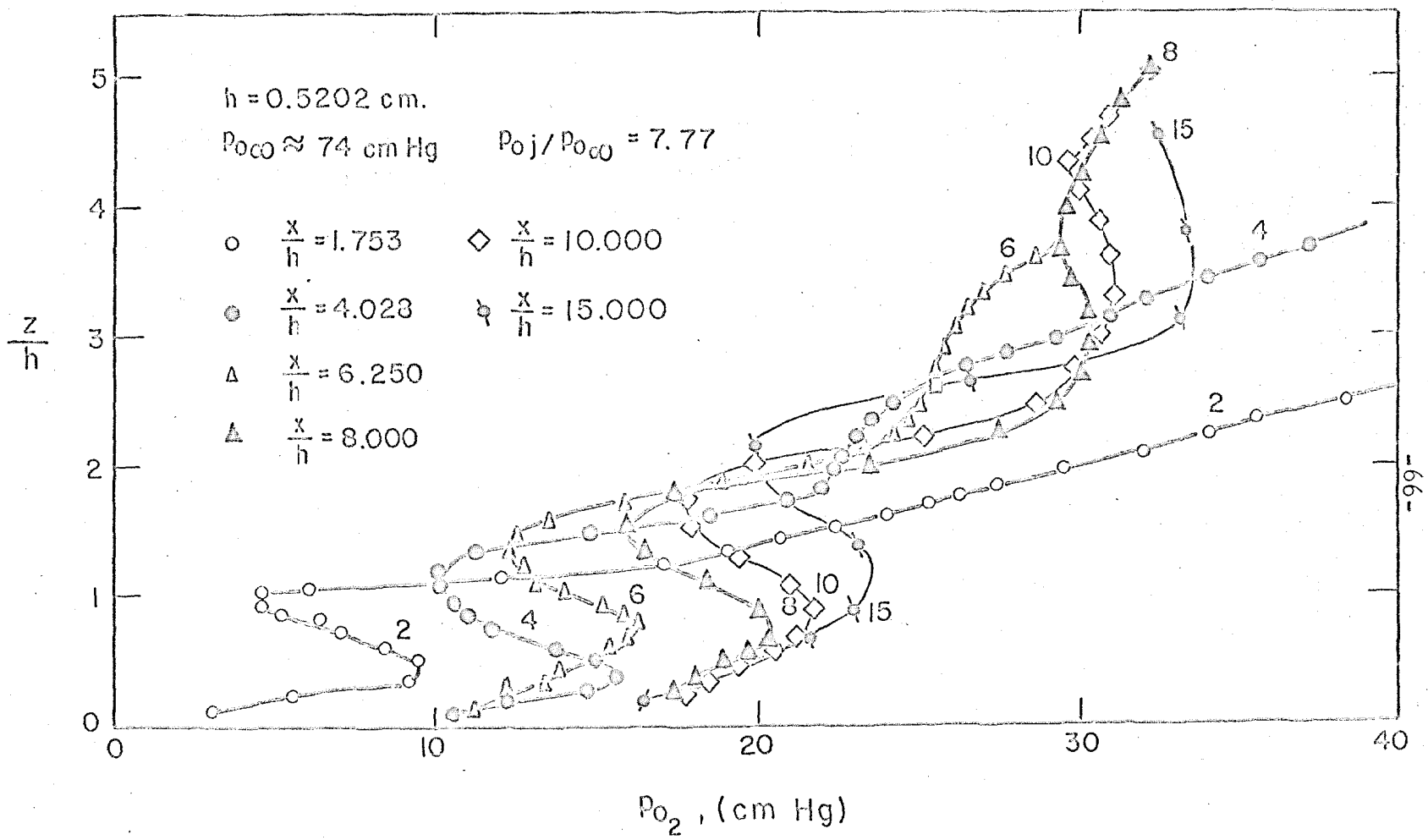

Fig. 29. Pitot Total Pressures at Various Axial Stations During Three-Dimensional Injection with a Turbulent Boundary Layer. $M_\infty = 2.610$.

APPENDIX A

Formulae:

1. $$\gamma = \frac{\sum_{i=1}^{2} m_i C_{p_i}}{\sum_{i=1}^{2} m_i C_{v_i}}$$

2. Rayleigh Supersonic Pitot Formula

$$\frac{p_{o_2}}{p_1} = \frac{\left(\frac{\gamma+1}{2} M^2\right)^{\frac{\gamma}{\gamma-1}}}{\left(\frac{2\gamma}{\gamma+1} M^2 - \frac{\gamma-1}{\gamma+1}\right)^{\frac{1}{\gamma-1}}}$$

3. $$\bar{m}_A = K_A(39.94) + (1 - K_A)(28.97)$$

$$\bar{m}_{He} = K_{He}(4.00) + (1 - K_{He})(28.97)$$

4. $$a_o = \sqrt{\gamma g \frac{R}{\bar{m}} T_o} = \left\{\begin{matrix} 5130 - A \\ 4740 - He \end{matrix}\right\} \sqrt{\frac{\gamma}{\bar{m}}} \quad ; \quad T_o = 530°R.$$

5. $$\frac{T_o}{T} = 1 + \frac{\gamma-1}{2} M^2$$

6. $$a = a_o \sqrt{\frac{T}{T_o}}$$

7. $$v = M a$$

8. $$\frac{p_o}{p} = \left(\frac{T_o}{T}\right)^{\frac{\gamma}{\gamma-1}}$$

9. $$\frac{p_o}{p_{o\infty}} = \frac{p_o}{p} \frac{p}{p_{o\infty}} \quad ; \quad p \text{ and } p_{o\infty} \text{ known}$$

10. For continuity of argon check in two-dimensional case:

$$d\dot{m}_A = K_A \rho v \, dz = K_A \frac{p \bar{m}}{R T_0} \frac{T_0}{T} \frac{V}{V_\infty} V_\infty h \, d\left(\frac{z}{h}\right)$$

$$d\dot{m}_A' = K_A p \bar{m} \frac{T_0}{T} \frac{V}{V_\infty} d\left(\frac{z}{h}\right)$$

$$\Delta \dot{m}_A' = \frac{1}{2}\left[K_{A_i} p_i \bar{m}_i \frac{T_0}{T_i} \frac{V_i}{V_\infty} + K_{A_{i+1}} p_{i+1} \bar{m}_{i+1} \frac{T_0}{T_{i+1}} \frac{V_{i+1}}{V_\infty} \right] \Delta \frac{z}{h}$$

$$\dot{m}_A' = \sum_{\frac{z}{h}=0}^{\frac{z}{h}(K_A=0)} \Delta \dot{m}_A'$$

TABLE A-I

Specific Heats and Ratio of Specific Heats as a Function of Injectant Concentration

$K(\%)$	$\sum_{i=1}^{2} m_i C_{p_i}$	$\sum_{i=1}^{2} m_i C_{v_i}$	γ	$K(\%)$	$\sum_{i=1}^{2} m_i C_{p_i}$	$\sum_{i=1}^{2} m_i C_{v_i}$	γ
0	7.00	5.00	1.400	27	6.46	4.46	1.448
1	6.98	4.98	1.402	28	6.44	4.44	1.450
2	6.96	4.96	1.403	29	6.42	4.42	1.452
3	6.94	4.94	1.405	30	6.40	4.40	1.455
4	6.92	4.92	1.406	31	6.38	4.38	1.457
5	6.90	4.90	1.408	32	6.36	4.36	1.459
6	6.88	4.88	1.410	33	6.34	4.34	1.461
7	6.86	4.86	1.412	34	6.32	4.32	1.463
8	6.84	4.84	1.413	35	6.30	4.30	1.465
9	6.82	4.82	1.415	36	6.28	4.28	1.467
10	6.80	4.80	1.417	37	6.26	4.26	1.469
11	6.78	4.78	1.418	38	6.24	4.24	1.472
12	6.76	4.76	1.420	39	6.22	4.22	1.474
13	6.74	4.74	1.422	40	6.20	4.20	1.476
14	6.72	4.72	1.424	41	6.18	4.18	1.478
15	6.70	4.70	1.426	42	6.16	4.16	1.481
16	6.68	4.68	1.427	43	6.14	4.14	1.483
17	6.66	4.66	1.429	44	6.12	4.12	1.485
18	6.64	4.64	1.431	45	6.10	4.10	1.488
19	6.62	4.62	1.433	46	6.08	4.08	1.490
20	6.60	4.60	1.435	47	6.06	4.06	1.493
21	6.58	4.58	1.437	48	6.04	4.04	1.495
22	6.56	4.56	1.439	49	6.02	4.02	1.498
23	6.54	4.54	1.441	50	6.00	4.00	1.500
24	6.52	4.52	1.442	51	5.98	3.98	1.503
25	6.50	4.50	1.444	52	5.96	3.96	1.505
26	6.48	4.48	1.446	53	5.94	3.94	1.508

K(%)	$\sum_{i=1}^{2} m_i C_{p_i}$	$\sum_{i=1}^{2} m_i C_{v_i}$	γ	K(%)	$\sum_{i=1}^{2} m_i C_{p_i}$	$\sum_{i=1}^{2} m_i C_{v_i}$	γ
54	5.92	3.92	1.510	85	5.30	3.30	1.606
55	5.90	3.90	1.513	86	5.28	3.28	1.610
56	5.88	3.88	1.575	87	5.26	3.26	1.613
57	5.86	3.86	1.518	88	5.24	3.24	1.617
58	5.84	3.84	1.521	89	5.22	3.22	1.621
59	5.82	3.82	1.524	90	5.20	3.20	1.625
60	5.80	3.80	1.526	91	5.18	3.18	1.629
61	5.78	3.78	1.529	92	5.16	3.16	1.633
62	5.76	3.76	1.532	93	5.14	3.14	1.637
63	5.74	3.74	1.535	94	5.12	3.12	1.641
64	5.72	3.72	1.538	95	5.10	3.10	1.645
65	5.70	3.70	1.541	96	5.08	3.08	1.649
66	5.68	3.68	1.543	97	5.06	3.06	1.654
67	5.66	3.66	1.546	98	5.04	3.04	1.658
68	5.64	3.64	1.549	99	5.02	3.02	1.662
69	5.62	3.62	1.552	100	5.00	3.00	1.667
70	5.60	3.60	1.556				
71	5.58	3.58	1.559				
72	5.56	3.56	1.562				
73	5.54	3.54	1.565				
74	5.52	3.52	1.568				
75	5.50	3.50	1.571				
76	5.48	3.48	1.575				
77	5.46	3.46	1.578				
78	5.44	3.44	1.581				
79	5.42	3.42	1.585				
80	5.40	3.40	1.588				
81	5.38	3.38	1.592				
82	5.36	3.36	1.595				
83	5.34	3.34	1.599				
84	5.32	3.32	1.602				

TABLE A-II

Mean Molecular Weights of Argon and Air and Helium and Air Mixtures as Functions of Concentrations

K (%)	$\overline{m}_{A+Air}$	$\overline{m}_{He+Air}$
0	28.97	28.97
5	29.52	27.72
10	30.07	26.47
15	30.62	25.22
20	31.16	23.98
25	31.71	22.73
30	32.26	21.48
35	32.81	20.23
40	33.36	18.98
45	33.91	17.73
50	34.46	16.48
55	35.00	15.24
60	35.52	13.99
65	36.10	12.74
70	36.65	11.49
75	37.20	10.24
80	37.75	8.99
85	38.29	7.75
90	38.84	6.50
95	39.39	5.25
100	39.94	4.00

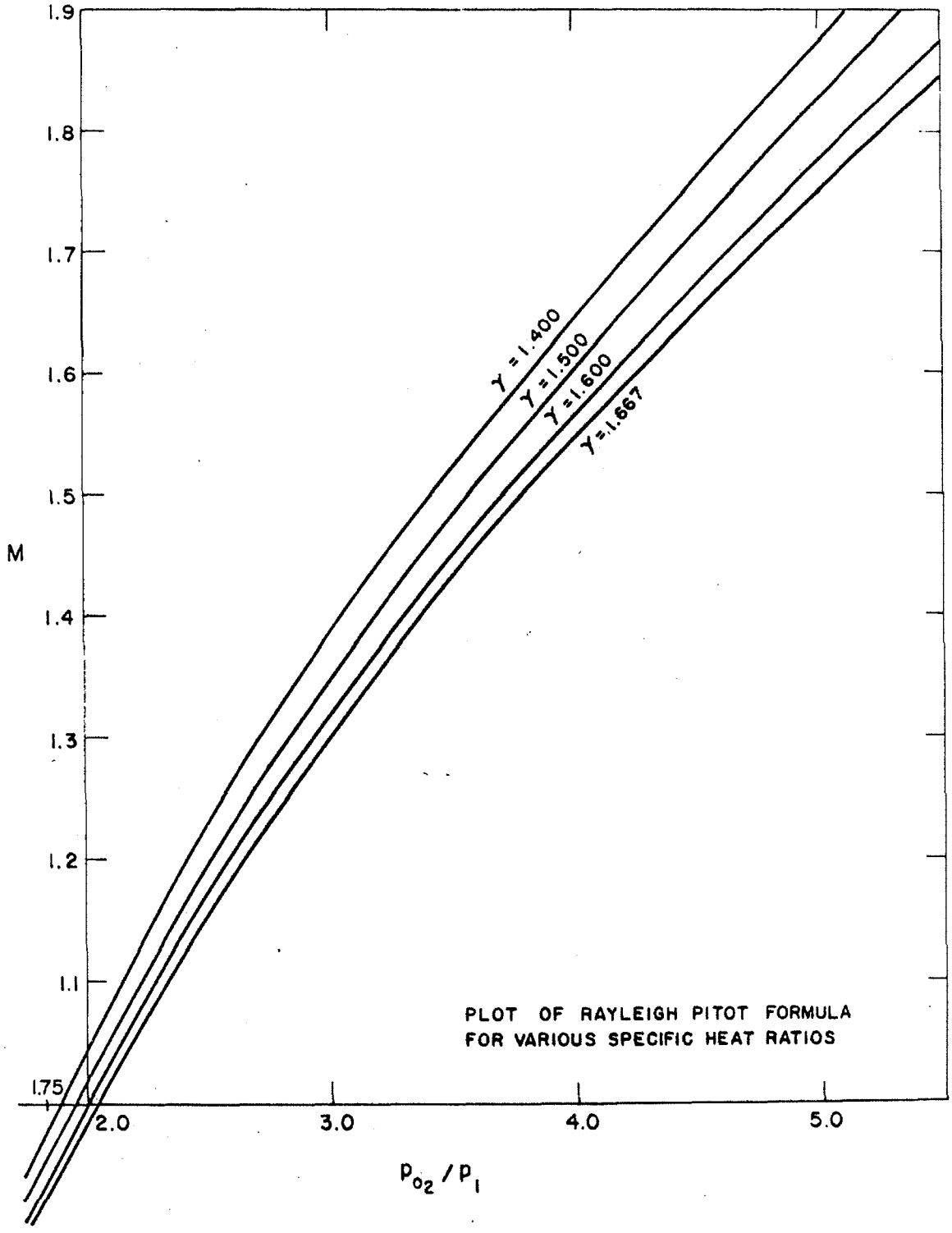
1.9
1.8
1.7
1.6
1.5
1.4
1.3
1.2
1.1
M
γ = 1.400
γ = 1.500
γ = 1.600
γ = 1.667
PLOT OF RAYLEIGH PITOT FORMULA
FOR VARIOUS SPECIFIC HEAT RATIOS
1.75
2.0
3.0
4.0
5.0
p_{o_2} / p_1

Figure A-1.

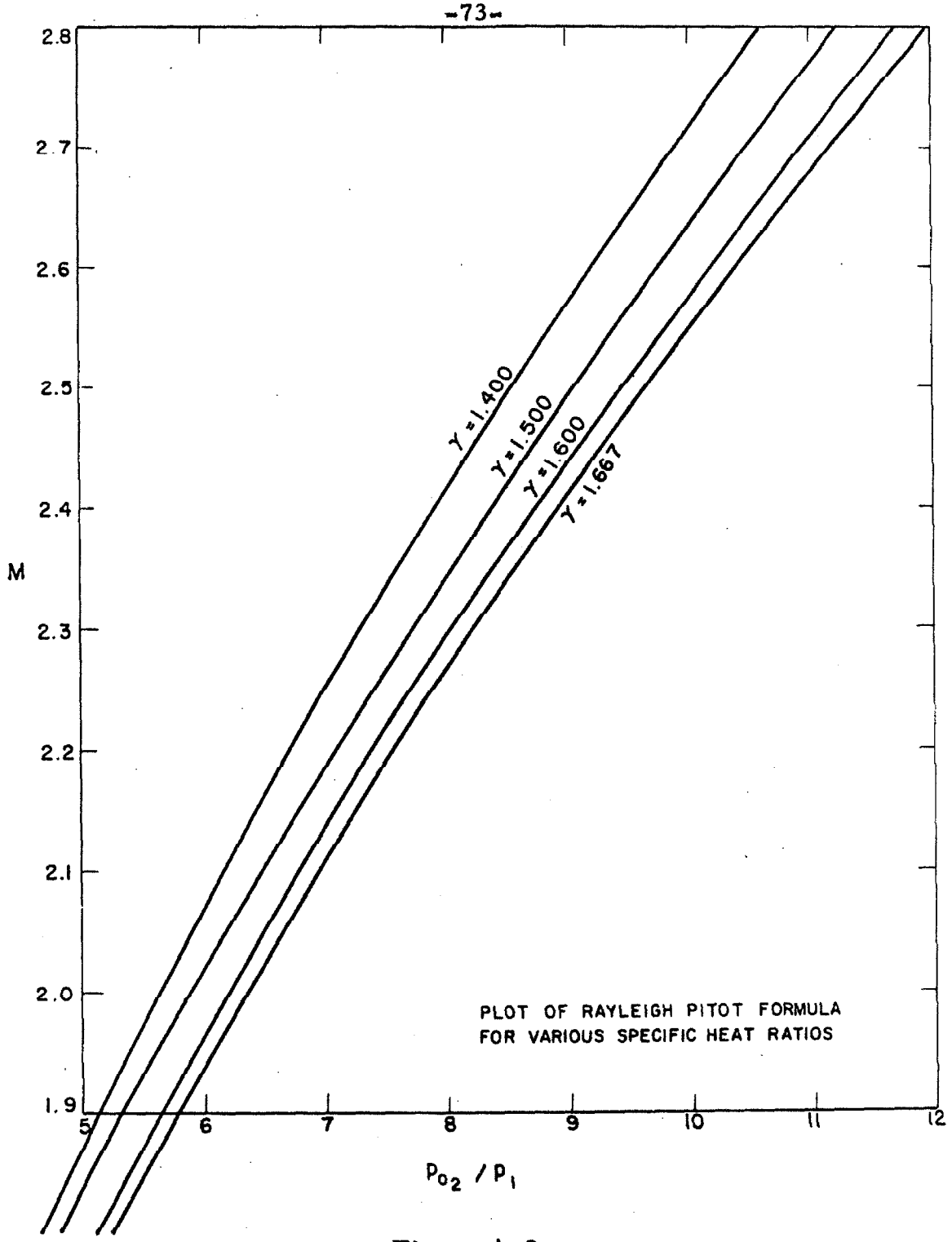
2.8
2.7
2.6
2.5
2.4
2.3
2.2
2.1
2.0
1.9
M
5
6
7
8
9
10
11
12
P_{o_2} / P_1
γ = 1.400
γ = 1.500
γ = 1.600
γ = 1.667
PLOT OF RAYLEIGH PITOT FORMULA
FOR VARIOUS SPECIFIC HEAT RATIOS

Figure A-2.

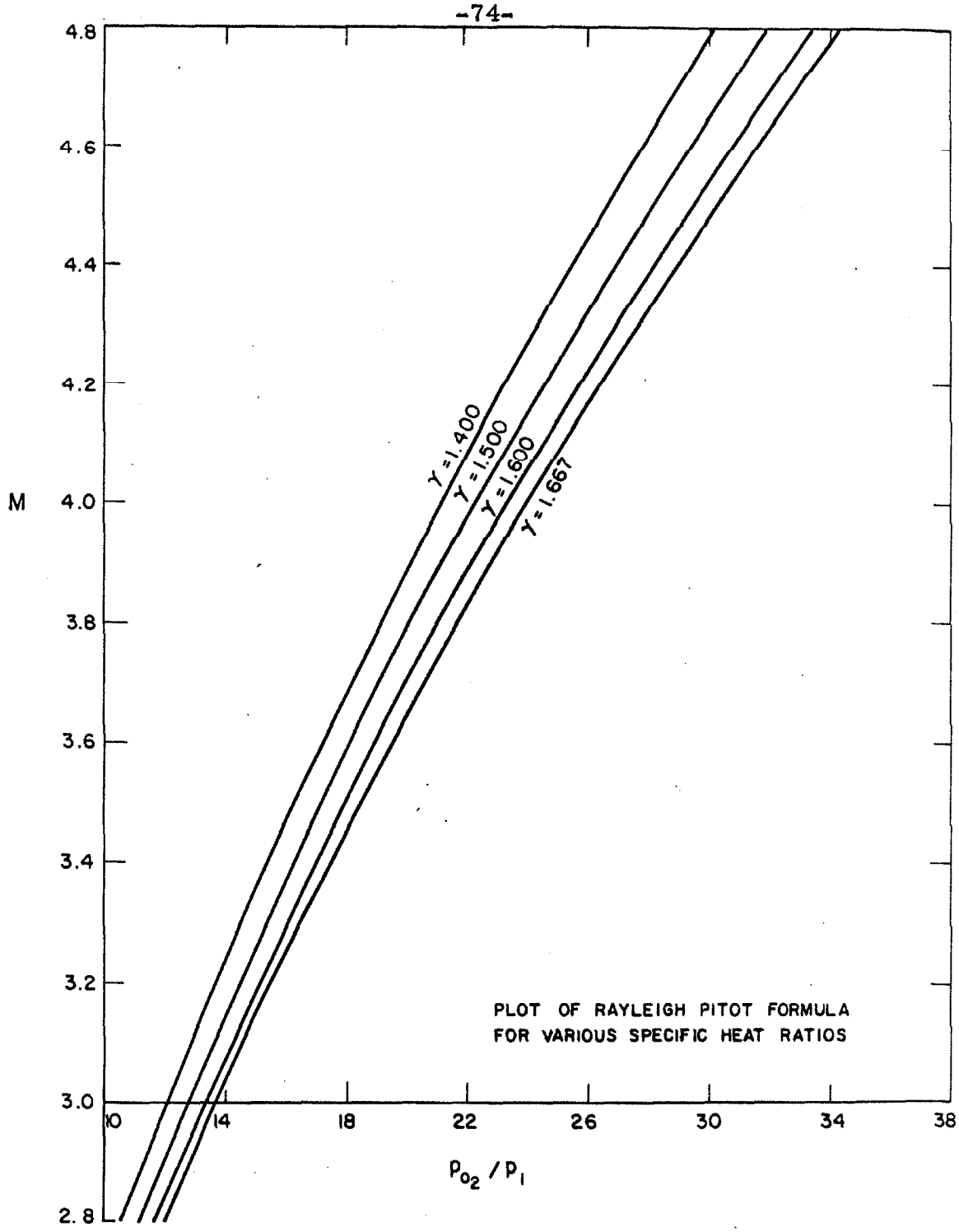
4.8
4.6
4.4
4.2
M
4.0
3.8
3.6
3.4
3.2
3.0
2.8
γ=1.400
γ=1.500
γ=1.600
γ=1.667
PLOT OF RAYLEIGH PITOT FORMULA
FOR VARIOUS SPECIFIC HEAT RATIOS
10
14
18
22
26
30
34
38
p_{o_2} / p_1

Figure A-3.

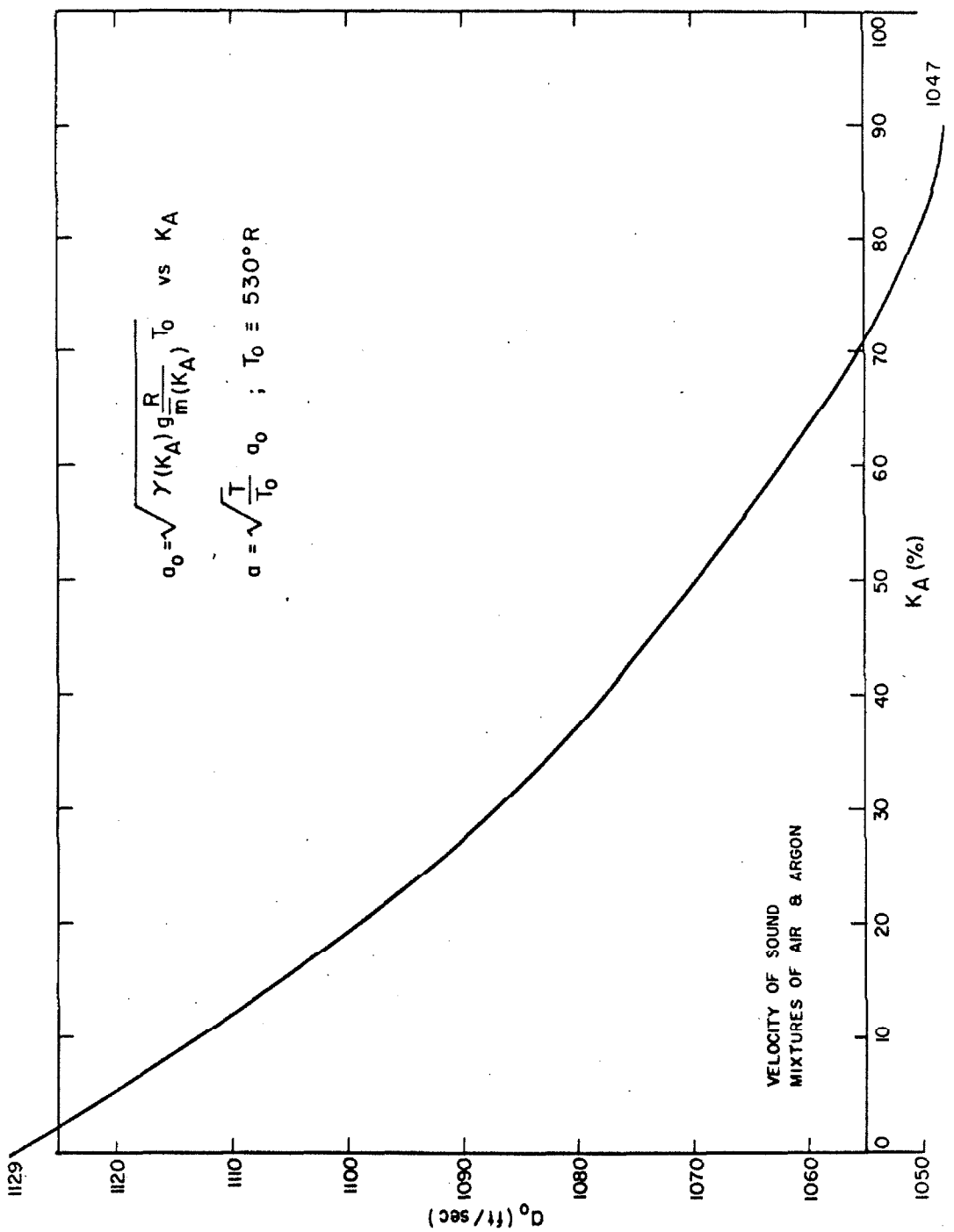
$a_o = \sqrt{\gamma(K_A) g \frac{R}{m(K_A)}} T_o$ vs K_A
$a = \sqrt{\frac{T}{T_o}}\, a_o$; $T_o = 530°R$
VELOCITY OF SOUND
MIXTURES OF AIR & ARGON
a_o (ft/sec)
K_A (%)
1129
1120
1110
1100
1090
1080
1070
1060
1050
1047
0
10
20
30
40
50
60
70
80
90
100

Figure A-4.

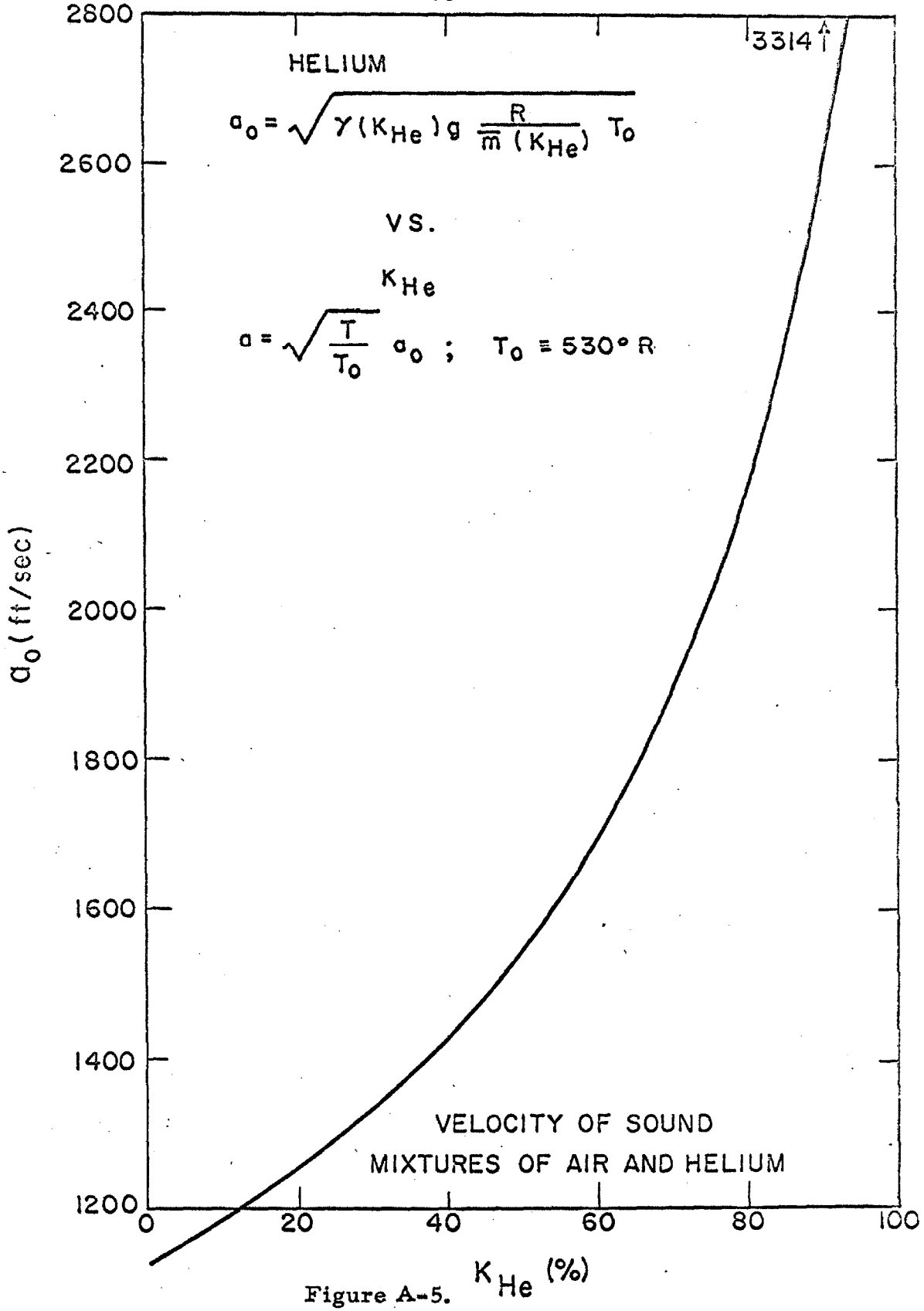
HELIUM
$a_o = \sqrt{\gamma(K_{He})\, g\, \frac{R}{\bar{m}(K_{He})}\, T_o}$
VS.
K_{He}
$a = \sqrt{\frac{T}{T_o}}\, a_o$; $T_o \equiv 530^\circ R$
3314
2800
2600
2400
2200
2000
1800
1600
1400
1200
a_o (ft/sec)
0
20
40
60
80
100
K_{He} (%)
VELOCITY OF SOUND
MIXTURES OF AIR AND HELIUM

Figure A-5.